Lower-hybrid drift waves and electromagnetic electron space-phase holes associated with dipolarization fronts and field-aligned currents observed by the Magnetospheric Multiscale mission during a substorm

O. Le Contel[1], R. Nakamura[2], H. Breuillard[1], M. R. Argall[3], D. B. Graham[4], D. Fischer[2], A. Retinò[1], M. Berthomier[1], R. Pottelette[1], L. Mirioni[1], T. Chust[1], F. D. Wilder[5], D. J. Gershman[6], A. Varsani[2], P.-A. Lindqvist[7], Yu. V. Khotyaintsev[4], C. Norgren[4], R. E. Ergun[5], K. A. Goodrich[5], J. L. Burch[8], R. B. Torbert[3], J. Needell[3], M. Chutter[3], D. Rau[3], I. Dors[3], C. T. Russell[9], W. Magnes[2], R. J. Strangeway[9], K. R. Bromund[6], H. Y. Wei[9], F. Plaschke[2], B. J. Anderson[10], G. Le[6], T. E. Moore[6] , B. L. Giles[6], W. R. Paterson[6], C. J. Pollock[6], J. C. Dorelli[6], L. A. Avanov[6], Y. Saito[11], B. Lavraud[12], S. A. Fuselier[8], B. H. Mauk[10], I. J. Cohen[10], D. L. Turner[13], J. F. Fennell[13], T. Leonard[5] , A. N. Jaynes[5]

Olivier Le Contel, olivier.lecontel@lpp.polytechnique.fr

[1]Laboratoire de Physique des Plasmas

(LPP), UMR7648, CNRS, Ecole

This article has been accepted for publication and undergone full peer review but has not been through the copyediting, typesetting, pagination and proofreading process, which may lead to differences between this version and the Version of Record. Please cite this article as doi: 10.1002/2017JA024550

Abstract. We analyse two ion scale dipolarization fronts associated with field-aligned currents detected by the Magnetospheric Multiscale mission dur-

Polytechnique, UPMC Univ Paris 06, Univ. Paris-Sud, Observatoire de Paris, Paris, France

[2]Space Research Institute, Austrian Academy of Sciences, Graz, Austria

[3]University of New Hampshire, Durham, NH, USA

[4]Swedish Institute of Space Physics, Uppsala Sweden

[5]Laboratory for Atmospheric and Space Physics, University of Colorado, Boulder, CO, USA

[6]NASA Goddard Space Flight Center, Greenbelt, MD, USA

[7]Royal Institute of Technology, Stockholm, Sweden

[8]Southwest Research Institute, San Antonio, TX, USA

[9]University of California, Los Angeles, CA, USA

ing a large substorm on August 10, 2016. The first event corresponds to a fast dawnward flow with an anti-parallel current and could be generated by the wake of a previous fast earthward flow. It is associated with intense lower-hybrid drift waves detected at the front and propagating dawnward with a perpendicular phase speed close to the electric drift and the ion thermal velocity. The second event corresponds to a flow reversal: from southwward/dawnward to northward/duskward associated with a parallel current consistent with a brief expansion of the plasma sheet before the front crossing, and with a smaller lower-hybrid drift wave activity. Electromagnetic electron phase-space holes are detected near these low-frequency drift waves during both events.

[10]Applied Physics Laboratory, The Johns Hopkins University, Laurel, MD, USA

[11]Institute for Space and Astronautical Science, Sagamihara, Japan

[12]Institut de Recherche en Astrophysique et Planétologie (IRAP), CNRS UMR5277/Université Paul Sabatier, Toulouse, France

[13]Space Sciences Department, The Aerospace Corporation, El Segundo, CA, USA

The drift waves could accelerate electrons parallel to the magnetic field and produce the parallel electron drift needed to generate the electron holes. Yet, we cannot rule out the possibility that the drift waves are produced by the anti-parallel current associated with the fast flows, leaving the source for the electron holes unexplained.

Keypoints:

- Dipolarization fronts associated with field-aligned currents are observed at the plasma sheet edge with a few ion inertial length scale
- Intense lower-hybrid drift waves are detected at the front and can accelerate electrons parallel to **B**
- Electromagnetic electron phase-space holes are detected near the lower-hybrid drift waves and could be a latter by-product of these

1. Introduction

Magnetospheric substorms participate in a global cycle of energy circulation during which, starting from the Sun, the energy is transported by the solar wind until reaching the Earth's magnetosphere. There, energy, mass and magnetic flux enter into the Earth's magnetosphere by different processes (magnetic reconnection, Kelvin-Helmholtz instability, pressure pulse, ...) and are accumulated mostly in the magnetotail leading to the formation of a thin current sheet. Triggered by solar wind perturbations or becoming spontaneously unstable, the magnetotail suddenly releases the stored energy as the magnetic configuration changes from tail-like (stretched) to more dipolar-like configuration (or in other words operating a large scale dipolarization). Particles are accelerated parallel and perpendicular to the magnetic field producing the polar auroras and increasing the ring current. Thus energy and precipitated particles are finally injected into the ionosphere and contribute to the global Earth's atmosphere/ionosphere energy balance [e. g., *Kennel*, 1995]. A large dynamic current system (substorm current wedge, SCW) is also established [*McPherron et al.*, 1973] associated with this change of magnetic configuration and with fast plasma transport along the magnetotail in both directions. Despite intensive investigations, the mechanism of the substorm onset is still a matter of debate. A fair and consensual statement is that some substorms can be triggered by mid-tail reconnection [e.g., *Birn and Hesse*, 1991; *Scholer and Otto*, 1991; *Baker et al.*, 1996; *Angelopoulos et al.*, 2008b] while others require near-earth tail current disruption mechanisms [e.g., *Lui et al.*, 1991; *Roux et al.*, 1991; *Lui et al.*, 2008; *Liu et al.*, 2012]. Intermittent fast plasma transport or "bursty bulk flow" can be associated with substorm activity or also occur during

quiet conditions although less frequently [*Baumjohann et al.*, 1990; *Angelopoulos et al.*, 1992]. These transient and localized flows contribute for a significant part to the energy, plasma and magnetic flux transport in the magnetotail [*Angelopoulos et al.*, 1992]. They are also associated with a sharp transient increase of the normal component of the magnetotail, called dipolarization front (DF), and preceded frequently by a smaller negative variation [*Ohtani et al.*, 2004; *Runov et al.*, 2009]. Their mechanism of formation is also strongly investigated, notably by numerical simulations. *Sitnov et al.* [2009] showed in a full-particle simulation with open boundaries that they could appear in the outflow region before the steady reconnection is established. On the other hand, it has been suggested that they could be produced by the ballooning/interchange instability [*Nakamura et al.*, 2002; *Pritchett et al.*, 2014]. DFs have been extensively studied close to the magnetic equator where the plasma pressure and perpendicular current are dominant and β, the ratio between plasma pressure and magnetic pressure, can be much larger than 1 [e.g., *Runov et al.*, 2009; *Sergeev et al.*, 2009; *Fu et al.*, 2012; *Schmid et al.*, 2011]. Various types of electrostatic and electromagnetic waves have been detected in association with DF and found to be able to accelerate or diffuse particles. Intense whistler wave emissions are reported behind the DF in the pile-up region [*Khotyaintsev et al.*, 2011; *Viberg et al.*, 2014] and are shown to vary at the ion time scale [*Breuillard et al.*, 2016]. Lower-hybrid drift (LHD) waves and electrostatic electron cyclotron harmonic waves are also detected at and after the front respectively [*Sergeev et al.*, 2009; *Zhou et al.*, 2009; *Khotyaintsev et al.*, 2011; *Divin et al.*, 2015]. Finally, DFs and fast flows provide favourable conditions to the generation of both electromagnetic [*Andersson et al.*, 2009] and electrostatic solitary waves [*Kojima et al.*, 1994; *Cattell et al.*, 2005; *Khotyaintsev et al.*, 2010; *Deng et al.*,

2010; *Wang et al.*, 2014] which could also play a role in the acceleration and dissipation processes. Based on the large data set provided by a constellation of satellites including the five THEMIS probes, *Angelopoulos et al.* [2013] suggested that DF could be the major contributors to the total energy dissipation during the substorm process. Indeed, during their propagation through the magnetotail they generate a thin current sheet around the vicinity of the magnetic equator with a thickness of the order of the electron skin depth and could produce a significant dissipation $\mathbf{j} \cdot \mathbf{E} > 0$. Furthermore, their motion through the magnetotail induced a local current system very similar to the large scale SCW [*Cao et al.*, 2010; *Liu et al.*, 2013; *Palin et al.*, 2015]. Other investigations, notably by numerical simulations, suggested that an important dissipation could also occur out of equator due to the associated field-aligned currents [e.g., *Birn and Hesse*, 2005; *Pritchett et al.*, 2014]. Therefore, the study of DF deserves to be extended to the regions farther from the magnetic equator where the influence of the field-aligned currents can be more important and introduce different mechanisms and instabilities. In this study, we analyse two DF-like signatures associated with fast flow, field-aligned currents and various plasma waves detected by the Magnetospheric Multiscale (MMS) mission [*Burch et al.*, 2016] while MMS was located out of the magnetotail equator in the southern hemisphere. The data set and overview of the event are described in section 2. DF structures and plasma waves are detailed in sections 3, 4 and 5. Results are discussed in section 6.

2. Data and event overview

2.1. Data

The present study is based on measurements of the comprehensive instrument suite of the MMS mission [*Burch et al.*, 2016; *Torbert et al.*, 2016]. Magnetic field measurements

are provided by the Flux Gate Magnetometers (FGM) with a sample rate of 128 samples per second (S/s) in burst mode and 16 S/s in fast survey mode [*Russell et al.*, 2016]. Three-dimensional quasi-static and high-frequency electric field measurements are performed by the Electric Double Probes (EDP) with 8192 S/s in burst mode and 32 S/s in fast survey mode [*Lindqvist et al.*, 2016; *Ergun et al.*, 2016]. The Search-Coil Magnetometer (SCM) ensures the three-dimensional measurement of the high-frequency magnetic fluctuations with same sampling rates in burst and survey modes as EDP [*Le Contel et al.*, 2016]. Electric and magnetic waveforms are digitized by the Digital Signal Processing (DSP) unit which also provides onboard spectra up to 8 kHz in magnetic and 256 kHz in electric every 8 s in fast survey mode [*Ergun et al.*, 2016]. The Fast Plasma Instrument measures the three-dimensional electron and ion distribution functions from 10 eV to 30 keV every 30 ms for electrons and every 150 ms for ions in burst mode, 4.5 s for both species in fast survey mode [*Pollock et al.*, 2016]. Proton distribution functions and moments are also provided by the Hot Plasma Composition Analyzer with a time resolution of 10 s [*Young et al.*, 2016]. Energetic particle measurements from 25 to 600 keV for electrons and from 45 to 600 keV for ions are provided by the Energetic Particle Detectors (EPD) instrument suite [*Mauk et al.*, 2016] which consists of two different instruments: the Energetic Ion spectrometer [*Mauk et al.*, 2016] and the Fly's Eye Energetic Particle Spectrometers [*Blake et al.*, 2016]. Time resolution of electron FEEPS measurements is 0.3 s in burst mode and 2.5 s in survey mode. Ion EIS and FEEPS measurements are produced at 2.5 s (1/8 of the spin period). In the next sections, burst mode data are used except for the overview for which mostly survey mode data are displayed.

2.2. Event overview

On August 10th, 2016 MMS was located at [-7.0, 2.3, 0.5] Earth radii (RE) in the geocentric solar ecliptic coordinate system (GSE) around 10:00 UT; this location corresponds to the pre-midnight sector of the near-Earth magnetotail. Two large substorms occurred around 08:00 and 10:00 UT as indicated by the auroral electrojet index which reached about 1300 and 1200 nT respectively (courtesy of Kyoto World data Center for Geomagnetism, http://wdc.kugi.kyotou.ac.jp/ae_provisional/201608/index_20160810.html). The configuration of the tetrahedron is shown in Figure 1 with an average distance between satellites of about 55 km. Figure 2 displays an overview of the large scale dipolarization event associated with the substorm expansion phase based on survey data recorded by MMS3. Panel (a) indicates that MMS was located in the southern hemisphere and away from the central plasma sheet as $B_x \sim -100$ nT. On panel (b) the elevation angle defined by $\theta_{\rm elev} = \arctan(B_z/\sqrt{B_x^2 + B_y^2})$ increases from 25 up to 45° consistent with a large scale change of the magnetic field configuration from a stretched magnetotail to a more dipolar configuration: a large scale dipolarization. Associated with this change, electron and ion differential fluxes (panels c-g) as well as electron density (panel h) and temperatures (panel i) increase due to the sudden entry from the edge of the plasma sheet into the the hotter central plasma sheet. A fast dawnward flow ($v_{i,y} \sim -400$ km/s) followed by a fast earthward and duskward flow ($v_{i,x} \sim v_{i,y} \sim +300$ km/s) are detected after 1001 UT (panel j). Note that here burst ion FPI velocity data have been used after a specific treatment and time averaged at 4.5 s to match the time resolution of electron moments in survey mode. Indeed, the ion spectrogram indicate that measurements are perturbed by penetrating energetic electrons (see Figure 2f after 1001 UT) which induce false counts at low

energy. This background noise has been removed in order to recover ion moments that match HPCA H^+ moments (Figure 2g). The background noise calculation is based on the assumption that the (five) lowest energy channels should not measure any particles. On the other hand, it is expected that the background counts does not depend on the energy. Thus, the average counts are calculated for these low-energy channels, and then this constant count is removed from all energy channels for each data sampling (150 ms). Through this dipolarization event, large field-aligned current signatures can be seen until 1009 UT on panel (k). Electric field fluctuations above 40 kHz associated with the auroral kilometric radiation (AKR) are detected from 0950 to 1009 UT on panel (l); the magnetic counterpart is missed as the sampling rate is limited to 8 kHz (panel m). The AKR already detected before the local onset around 1001 UT is probably associated with the first substorm and produced by the corresponding auroral electron precipitations [e. g., *Pritchett and Strangeway*, 1985; *Ergun et al.*, 1998; *Strangeway et al.*, 1998]; it indicates that the magnetosphere is very perturbed and has never reached a relatively quiet steady state during the whole period. At lower frequencies, strong electric and magnetic field fluctuations are detected up to the electron gyrofrequency $f_{ce} = eB/(m_e 2\pi)$ (represented by the white line around 3 kHz) after the dipolarization begins. Note that most intense magnetic fluctuations (panel m) are measured below the lower-hybrid frequency $f_{LH} \sim \sqrt{f_{ce} f_{ci}}$ (dashed line around ~ 80 Hz).

Based on a multi-mission study including GOES, THEMIS, Van Allen Probes, Geotail and MMS satellites as well as ground-based measurements *Nakamura et al.* [2017] carried out a large-scale study of this substorm event. In particular, they showed that four field-aligned current (FAC) signatures were detected accompanied by dipolarization fronts

(increase of B_z or of the elevation angle) at 1001:22, 1001:43, 1002:41 and 1003:01 UT. The first FAC was flowing in the direction anti-parallel to **B** and towards the ionosphere while the last three were directed parallel and flowing out from the ionosphere (upward field-aligned current). The four FAC signatures were associated with strong dawn-to-dusk electric fields (> 10 mV/m) and large variations of the azimuthal velocity (dawn-dusk direction) as we have already noted on panel (j). In the following sections we will analyse in detail and at smaller scales the first two events associated with a reversal of the azimuthal ($\sim v_y$) plasma velocity.

3. Dipolarization front like signatures

DF have been mostly observed close to the magnetic equator ($B_x \sim 0$) by the previous missions; the sharp increase of the B_z component often preceded by a small decrease are the dominant variations reported during DF crossings [e. g., *Ohtani et al.*, 2004; *Runov et al.*, 2009]. In the present events, the MMS satellites are located far from the equator at the edge of the plasma sheet. In such conditions, the B_z variation cannot be sufficient to indicate the dipolarization of the fast moving plasma sheet flux tubes as the B_x component is dominant and can strongly vary too. The elevation angle shown in Figure 2a allows us to confirm that the B_z increase is effectively related to the dipolarization of the magnetic field lines. For the sake of simplicity, only the B_z variations will be shown hereafter.

Figure 3 shows in burst mode the first two dipolarization front-like signatures as indicated by the two successive increases of the B_z component (panel a). These signatures are also associated with two successive increases of the electron density (panel b) as the MMS4 satellite enters more deeply into the central plasma sheet. The first DF is associated with a field-aligned current reversal from anti-parallel (towards the ionosphere

or downward) to parallel (towards the tail or upward from the ionosphere) whereas the second is mainly related to a large parallel current (panel c). These currents are mainly carried by electron parallel velocities as we can see on panel (g). The first DF is associated with a fast dawnward plasma flow as both ions and electrons have large $v_{y,i} \sim -400$ km/s and $v_{y,e} \sim -1500$ km/s (panels e and g). The second event corresponds to an earthward $v_{x,i} \sim +100$ km/s, duskward $v_{y,i} \sim +200$ km/s and northward $v_{z,i} \sim +200$ km/s flow preceded by a short duration tailward ($v_{x,i,e} < 0$), dawnward ($v_{y,i,e} < 0$) and southward ($v_{z,i,e} < 0$) flow consistent with a brief expansion of the plasma sheet before the DF crossing. Electron velocities are much larger and are responsible for the large measured currents as mentioned before. Note that in Figure 3, ion and electron moments (in burst mode) have been time-averaged at 300 ms in order to reduce the noise on the FPI measurement (in addition to the specific treatment applied to ion moment described in the previous section) due to the low density (low count) condition at the edge of the plasma sheet. Still, ion velocities are probably underestimated due to the fact that in the plasma sheet a part of the ion distribution function is above the upper limit energy (30 keV) of FPI. Both events are accompanied by ion (panel d) and electron (panel f) dispersionless injections although they are not always time-aligned. For the first event, the maximum energy of injected ion is about 150 keV (dark blue line) and 300 keV (yellow/orange lines) for the second. For both events, electrons are injected up to the maximum energy ~ 500 keV suggesting a more efficient mechanism of acceleration and confirming the existence of high fluxes of penetrating energetic electrons mentioned in section 2. Comparison between the electric drift velocity $(\mathbf{E} \times \mathbf{B})/B^2$ and particle velocities perpendicular to $\mathbf{B}$ shows that for both events electrons are moving with the magnetic field lines while ions can be decoupled

at the front. Indeed, although parallel currents are dominant, perpendicular currents just at the front are sufficient to produce a significant Hall field able to decouple the ions. Furthermore, it indicates that the front thickness should be of the order of the ion skin depth $d_i = c/\omega_{pi}$ ($\omega_{pi} = \sqrt{e^2 n_0/m_i\epsilon_0}$ being the ion plasma frequency). This is confirmed by the estimation of the Hall field $\mathbf{j} \times \mathbf{B}$ obtained from curl of $\mathbf{B}$ (not shown). Discrepancies between electric drift and electron perpendicular velocity along x and z around 1001:28 UT are not significant as the FPI error bar on v_e is about 500 km/s at this time [*Gershman et al.*, 2015]. On the other hand, discrepancies between electric drift and ion perpendicular velocity are mostly real as the FPI error bars on v_i are always smaller than 250 km/s. Considering that the front crossing lasts about 1 s for the first event (3 s for second) due to the fast dawnward motion in the y direction, a rough estimate of the front thickness as well as the scale of the density gradient is about 1500 km or $2d_i$ for the first event (with $v_{\perp y,e} \sim -1500$ km/s and n$\sim$ 0.12 cm^{-3}) and also $\sim$ 1500 km for the second event (with $v_{\perp x,e} \sim v_{\perp z,e} \sim -500$ km/s). Based on a timing analysis, *Nakamura et al.* [2017] gave more precise estimates of the current sheet thickness associated with these DFs and found 1310 km and 710 km, respectively. Therefore, the spatial scale of these fronts crossed out of equator are about the ion inertial length, similar to those calculated closer to the magnetic equator by previous missions [e.g., *Runov et al.*, 2009; *Zhou et al.*, 2009; *Deng et al.*, 2010; *Khotyaintsev et al.*, 2011].

Figure 4 shows in detail the first DF (from MMS4 data) associated with an increase of the B_z component (panel a), a decrease of the magnitude of the magnetic field while the density increases as expected for a pressure balance between magnetic pressure and plasma thermal pressure in the plasma sheet. Electric (panel d) and magnetic (panel

e) waveforms are plotted in magnetic field-aligned (MFA) coordinates with the z_{MFA} axis (red curve) directed along the background magnetic field defined as a 0.03 s time-average of $\mathbf{B}$, $\mathbf{x}_{\mathrm{MFA}}$ (blue curve) given by $-\mathbf{z}_{\mathrm{MFA}} \times \mathbf{y}_{\mathrm{GSE}}$ and $\mathbf{y}_{\mathrm{MFA}} = \mathbf{z}_{\mathrm{MFA}} \times \mathbf{x}_{\mathrm{MFA}}$ (green curve). Waveforms have been band-pass filtered between 32 Hz and 4 kHz. The perpendicular electric component (green) is dominant and reaches ±200 mV/m whereas the parallel (red) magnetic component reaches ±0.2 nT. Fourier spectra of the electric and magnetic fluctuations are calculated with 256 points, a hanning window and without time overlapping (panels f and g). While electric fluctuations can be broad band up to f_{ce}, magnetic fluctuations are mainly below the lower hybrid frequency as already noted in Figure 1. On panel (h) a reversal of the parallel component of the Poynting vector occurs; the first part of the fluctuations propagates parallel to $\mathbf{B}$ and towards the tail whereas the second part propagates earthward towards the ionosphere. Associated with these fluctuations, a sudden increase of the parallel electron temperature is measured (panel i) as well as an anti-parallel current up to -100 nA.m^{-2} (panel j). Finally, from the last three panels (k-m) showing electron energy–time spectrograms parallel, perpendicular and anti-parallel to $\mathbf{B}$, an excess of parallel fluxes is measured, consistent with the peak of the anti-parallel current.

Figure 5 shows the same observations recorded on MMS3 during the second DF crossing. Same increase of the B_z component (panel a), decrease of B (panel b) and increase of the electron density (panel c) are measured as for the first event. Four enhancements of the wave activity are detected around 1001:41.500, 1001:43.500, 1001:46.000 and 1001:48.000 UT (panels d and e). However, only the first enhancement corresponding to the largest and longest duration perpendicular electric field fluctuations ($\sim \pm$50mV/m)

is accompanied by a clear positive parallel component of the Poynting vector (panel h) and an increase of the parallel electron temperature (panel i). While the second and third enhancements are associated with large positive parallel currents (~ 100 nA.m^{-2}, panel j), the first correspond to a small anti-parallel current (~ -25 nA.m^{-2}) and the fourth to a field aligned current reversal ($\sim +25/-25$ nA.m^{-2}). Finally, the electron energy–time spectrograms (panels k-m) show that the first enhancement of the wave activity associated with the increase of the parallel electron temperature is also associated with an excess of parallel fluxes.

In the next section, the electric and magnetic fluctuations with frequencies below and near f_{LH} are analysed in detail.

4. Lower-hybrid waves

Adopting the method developed by *Norgren et al.* [2012]; *Divin et al.* [2015] for analysing plasma waves with $f_{ci} \ll f \sim f_{LH} \ll f_{ce}$ (with $2\pi f_{LH} = \omega_{pi}/\sqrt{1+\omega_{pe}^2/\omega_{ce}^2}$), we assume that only electrons are magnetized. Therefore the wave perpendicular current can be obtained from the electron electric drift as $-en_0(\delta\mathbf{E}\times\mathbf{B_0})/B_0^2$ assuming that ions are stationary at this short time scale. Then from the Ampère's law and assuming a quasi-electrostatic field $\delta E_\perp \sim ik_\perp\delta\phi$, we obtain the following estimate of the electrostatic potential $\delta\phi = B_0\delta B_\parallel/(en_0\mu_0)$. On the other hand, the electrostatic potential can be directly obtained by the integration of the perpendicular electric field (which is the dominant component) along the direction of the propagation $\delta\phi = \int \delta\mathbf{E}_\perp\cdot\mathbf{v}_{\perp,ph}dt$ where $\mathbf{v}_{\perp,ph}$ is the perpendicular phase speed. Then we proceed in two steps: (i) the direction of propagation is found by doing cross-correlations between the two estimates of the electrostatic potential for different angles of propagation (in the plane perpendicular to $\mathbf{B}$), (ii) the amplitude is

determined by fitting the amplitude of the two potentials. Note that the average frequency of the fluctuations is also determined from the two nearest extremas of the correlation coefficient.

Figure 6 shows the results of this analysis for the 4 satellites between 1001:27.400 and 100128.800 UT. Best correlation rates are obtained from $\delta E_\perp$ (black curve) and $\delta B_\parallel$ (red curve) waveforms band-pass filtered around the estimated $\mathrm{f}_{LH} \sim 60$ Hz from 32 to 300 Hz and limited between 1001:27.850 and 100128.250 UT. These fluctuations are associated with density and parallel temperature jumps; MMS3 being the first to measure these jumps as well as the electrostatic potential fluctuations. Table 1 shows that frequency ($\sim 54.6 - 68.3$ Hz), phase speed (~ -1217.6 to -1091.3 km/s), perpendicular wavelength $\lambda_\perp$ ($\sim 17 - 20$ km) estimates are very close for all satellites. To summarize, these fluctuations have frequencies close to f_{LH}, are propagating perpendicular to $\mathbf{B}$ mostly towards the dawn with a phase speed about -1150 km/s, a fraction of the electric drift, and with $\mathrm{k}_\perp \rho_e \sim 0.5$. Note that for such a large $k_\perp$, a strong Doppler-shift effect is expected ($k_\perp v_{\perp,i} \sim \omega_{LH}$) resulting in broader band spectra already noted by *Huba et al.* [1978] for distant magnetotail conditions. The ratio between the electrostatic potential and the electron temperature between 0.22 and 0.36 indicates that these fluctuations are sufficiently powerful to modify the electron distribution function.

During the detection of these fluctuations, electrons are frozen-in and drifting dawnward at about -1500 km/s in the spacecraft frame while ions have a velocity of -400 km/s (Figure 3, panels d, e, g). For both species, we can write in the spacecraft frame $v_{y,j} = v_{E,y} + v_{dia,j}$ for $j = i, e$ where v_E denotes the electric drift and $v_{dia,j} = -T_j/(m_j \omega_{cj}) \nabla[(\ln n_0 T_j)]$ is the diamagnetic drift. Yet, from data $v_{y,e} \sim v_{E,y}$

so electron diamagnetic velocity can be neglected (T_e ¡T_i) and $v_{E,y} \sim v_{th,i}$ ($v_{th,i}$ is the ion thermal velocity and for $T_i \sim 7$ keV, $v_{th,i} \sim 1200$ km/s). For ions, $v_{y,i} = v_{E,y} + v_{dia,i}$ leading to $v_{dia,i} = v_{y,i} - v_{E,y} \sim v_{th,i} \sim 1100$ km/s; with $v_{dia,i} \sim v_{th,i}$, the density gradient length scale is about the ion Larmor radius. In the limit $v_{y,i} \ll v_{E,y}$, we would have $v_{dia,i} \sim -v_{E,y}$. However, the ion diamagnetic velocity could be overestimated as $v_{y,i}$ is probably underestimated due to the fact that in the plasma sheet a part of the ion distribution function is above the upper limit energy (30 keV) of FPI. Neglecting this possible effect, the electron-ion drift velocity between ion and electrons is about 1100 km/s and corresponds to the ion diamagnetic drift due to the ion pressure gradient and is also close to the electric drift $v_{E,y}$.

Based on a linear kinetic theory *Davidson and Gladd* [1975] demonstrated that for $v_{E,y} \sim v_{th,i}$, $k_\parallel = 0$ (flute-like perturbation), T_e/T_i=0.2 and $\beta_e = 0.04$, the maximum growth rate of the lower-hybrid drift instability is about $0.2\omega_{LH}$ for $k_\perp \rho_e (T_i/T_e)^{1/2} \sim 1$ and $v_{ph} = \omega/k_\perp \sim 0.5 v_{E,y}$ (see their Figure 2 for more details); these plasma conditions are very similar as those of this event (corresponding to $T_e/T_i \sim 0.4$, $\beta_e \sim 0.01$).

Table 2 summarizes the wave properties during the largest and longest duration electric field fluctuations associated with the sharp increases of the parallel electron temperature and density; these waves were detected around 1001:41.100 UT, just before the second DF crossing (see Figure5d, e, i). As the electric field amplitudes are smaller and the waveform is less monochromatic than for event 1, correlation rates are quite smaller (~ 0.6 instead of ~ 0.9). Another probable reason which is investigated in the next section, is the fact that smaller scale solitary structures are now superposed to the LHD waves. Despite these differences, frequencies (from 45 to 68 Hz), perpendicular phase speeds (from -770

to -551 km/s) and wavelengths (from 8 to 14.7 km) are quite similar as for the first event. The electron velocity in the y direction on MMS3 is still equal to the electric drift and about - 1000 km/s while ion velocity is only ~ -250 km/s leading to an electron-ion drift about ~ 750 km/s (see Figure 3i). Consistently, the estimated perpendicular phase speed is also smaller than for event 1 and close to this electron-ion drift velocity. Note that for these fluctuations, the ratio between the electrostatic potential and the electron temperature is ~ 0.05 therefore much smaller than for the first event although a sudden increase of the parallel electron temperature is also measured.

All these properties allow us to identify these fluctuations as lower-hybrid drift waves produced by the LHD instability which has its maximum growth rate in such conditions and propagate at a phase speed close to $v_{E,y} \sim v_{th,i}$.

Finally, on Figure 4d, e we can see that these LHD waves are followed by electromagnetic solitary structures while for the second event on Figure 5d, e same solitary signatures are detected before and during the LHD wave emission. The next section is dedicated to the analysis of these solitary structures.

5. Electromagnetic electron space-phase holes

Figure 7a-d displays the three components and the magnitude of the magnetic field obtained from the merged product between FGM and SCM data about 500 ms after the LHD wave emission associated with the first DF. This data set has been obtained by merging FGM and SCM data in a common sensor frame and taking into account the frequency response of each instrument [*Fischer et al.*, 2016].

This merged product allows us to identify a train of solitary magnetic structures while keeping the information about the location of the satellites from the DC part of the

magnetic field ($\sim B_x$), some of them being detected by different satellites at the same time, others being only detected by one satellite. For instance, at 1001:28.566 UT a bump of about 0.2 nT in the magnetic field is detected by MMS1, MMS3 and MMS4 but missed by MMS2 while large bumps between 100128.620 and 100128.640 are only detected by MMS3. Note that from the DC magnetic field measurement, we can see that MMS2 measures a quite different magnetic field than the others due to its separation in y (Figure 1) which indicates that both DF and solitary structures are relatively localized in the y direction and that the solitary waves propagate along the magnetic field lines mostly in the (x, z) plane. Figure 7e shows the parallel electric field obtained by using DC-coupled EDP data at 8192 S/s and the survey magnetic field data; the bipolar signatures are well above the measurement uncertainty, which is about ± 8 mV/m during this period, and are time-aligned with the magnetic solitary field perturbations. An important point is that all large bipolar signatures correspond to positive then negative polarity. This suggests that they are produced by a positive charge excess or in others words, an electron space-phase hole (denoted EH hereafter), which would propagate along the magnetic field in the tailward direction and from the same source region. We can rule out the alternative interpretation also consistent with a positive charge excess, an ion packet, since having an ion scale larger than the MMS satellite separation ($\sim 55 < \rho_i \sim 100$ km), it would be detected by the four spacecraft at the same time. Finally, it is worth noting that the amplitude of the bipolar signatures as well as those of the magnetic field bumps which are only detected by MMS3 after 1001:28.620 UT decrease with the decrease of the background magnetic field (see panels d and e) suggesting that a relaxation process is on-going.

Such electromagnetic solitary structures with the same polarity were already detected by one probe of the THEMIS mission in very similar conditions. Indeed, their detection was associated with the crossing of a fast earthward ($\sim$ 1000 km/s) and dawnward (~ -800 km/s) flow while THEMIS A was located in the edge of the plasma sheet in the southern hemisphere [*Andersson et al.*, 2009; *Tao et al.*, 2011]. Figure 7f-g shows the electric drift measured in the spacecraft frame. Panel (g) reminds that these structures are detected during a fast background dawnward flow at ~ -1200 km/s but indicates that the perpendicular electric field of the solitary structures is strong enough to modify locally the electric drift. In order to study in detail the internal structure of these electromagnetic solitary waves, we zoom in on the single structure detected by three MMS satellites at 1001:28.566-567 UT (Figure 8).

Now, the magnetic and electric waveforms have been band-pass filtered between 32 Hz and 4 kHz and moved into the magnetic field-aligned coordinate system (panels a-f) and the electric drift ($\delta\mathbf{E} \times \mathbf{B}_0^2/B_0^2$) is calculated with the two perpendicular components of the band-pass filtered electric field and the background magnetic field (panels g, h). The structure is detected at the same time by MMS4 and MMS3 then 1.0 ms later by MMS1 which, taking into account of the MMS configuration, gives a velocity $\sim 45 \times 10^3 - 55 \times 10^3$ km/s in the tailward direction; such a velocity is of the same order (1.2-1.5) of the electron thermal velocity $v_{th,e} \sim 37 \times 10^3$km/s (for $T_e \sim 4$ keV) and $0.15 - 0.18$ the speed of light c. We can also estimate the velocity of these structures from the Lorentz transformation [*Andersson et al.*, 2009] which yields (assuming that the perpendicular magnetic components vanish in the rest frame) to:

$$\delta B_y = \frac{v_{EH}}{c^2}\delta E_x$$

$$\delta B_x = -\frac{v_{EH}}{c^2}\delta E_y \tag{1}$$

and gives $v_{EH} = c^2\delta B_y/\delta E_x \sim 67.5 \times 10^3$ km/s with $\delta B_y = -0.12$ nT and $\delta E_x = -160$ mV/m (positive v_{EH} means parallel to $\mathbf{B}_0$ and towards -x$_{GSE}$) from MMS1 measurements; the second equation gives $v_{EH} = -c^2\delta B_x/\delta E_y \sim +100 \times 10^3$ with $\delta B_x = -0.1$ nT and $\delta E_y = 90$ mV/m. This large value compared with the previous estimations is likely due to the fact we have neglected the perpendicular magnetic components in the rest frame which can lead to an overestimation of v_{EH} as described by *Tao et al.* [2011]. Considering only the first two estimates, both observational and theoretical values give $v_{EH} \sim 1.2 - 1.8 v_{th,e} \sim 0.15 - 0.22c$ which is very similar to the values found by *Andersson et al.* [2009] or *Tao et al.* [2011]. Note that this EH signature has also been recorded in high-speed burst mode (with 16384 S/s for SCM and 65384 S/s for EDP) and the same amplitudes were measured (not shown), indicating that the structure is already well sampled in burst mode. Yet, some interferences are present at high-frequency which makes burst mode data preferable. Next, the parallel length scale of the electron hole $L_\parallel$ can be easily estimated as $v_{EH} \times dt \sim 45 - 60$ km (dt being the duration of the bipolar signature ~ 1 ms) very close to the mean value of 68 km found by *Tao et al.* [2011]; this value is about 33-44λ_{De} (where $\lambda_{De} \sim 1.35$ km for $n_0 \sim 0.12$ and $T_e \sim 4$ keV). The perpendicular scale $L_\perp$ must be smaller than 55 km since MMS2 missed the electron hole therefore $L_\perp \leq L_\parallel$. This latter conclusion is consistent with those drawn by *Andersson et al.* [2009] based on the fact that the perpendicular electric field components were larger than the amplitude of the bipolar parallel electric field. However, here we observe both cases as MMS3 and MMS4 have larger parallel electric field than perpendicular whereas it is the

opposite on MMS1. We cannot determine if this difference is due to the time evolution or to a different trajectory through the electron hole. Yet, we can assume that if a spacecraft crosses the electron hole close to its symmetry axis it would measure a larger parallel electric field than a perpendicular electric field whereas the opposite would be expected if it crosses the structure only at the edges as noted by *Andersson et al.* [2009]. On the other hand, for these electromagnetic structures, by symmetry the largest perturbation of $\delta B_{\parallel}$ is expected for the satellite the closest to the central axis. Therefore, we can assume that MMS4, which measures the largest $\delta B_{\parallel}$, is the closest to the central axis; it measures also a parallel electric component two times larger than the perpendicular component. At the same time, MMS3 measures a smaller $\delta B_{\parallel}$ and a larger δE_y consistent with a location farther from the central axis. Neglecting a possible time variation, signatures on MMS1 are also consistent with a crossing farther from the central axis. Furthermore, we can note that MMS4 and MMS1 have the same negative polarity for δB_x and δB_y whereas MMS3 has the opposite polarity (¿0) suggesting that they are located at opposite positions with regard to the central axis. The same remark can be made about the perpendicular electric component, MMS1 and MMS4 having negative polarity for δE_x and positive for δE_y whereas MMS3 measures the opposite polarities. All these observations are consistent with a cylindrically symmetric potential structure [*Andersson et al.*, 2009; *Tao et al.*, 2011; *Treumann and Baumjohann*, 2012].

The electron Larmor radius being of the same order of λ_{De} and the time scale of the structure (1 ms) being longer than the electron gyroperiod, the assumption that electrons can be magnetized inside the electron hole is realistic. Indeed, electromagnetic electron space-phase holes have been modelled by assuming that the $\delta B_{\parallel}$ perturbation was induced

by a current from $\delta\mathbf{E} \times \mathbf{B}_0$ drift of electrons passing through the solitary structure [*Tao et al.*, 2011] or trapped in it [*Treumann and Baumjohann*, 2012] while ions were assumed stationary. We can estimate the current produced by the electron drift plotted on Figure 8g, h, we get $\delta J_y \sim -en_0(\delta\mathbf{E} \times \mathbf{B}_0)_y/B_0^2 \sim 25$ nA/m^2 which is a quite significant current compared with the large-scale perpendicular current shown in Figure 3c. *Tao et al.* [2011] computed the parallel magnetic field perturbation along the axis induced by the electron electric drift and obtained $\delta B_\parallel = en_0\mu_0 V_0/B_0 g(l_\perp/l_\parallel)$ where V_0 is the electrostatic potential on the central axis and $g(l_\perp/l_\parallel)$ is a shape factor depending on the ratio $l_\perp/l_\parallel$. Taking $n_0 = 0.12$ p.cm^{-3}, $V_0 \sim 1.1$ kV (with $E_\parallel \sim 130$ mV/m and $L_\parallel \sim 55$ km, $B_0 = 120$ nT and g=0.7 (assuming $l_\perp \sim l_\parallel$), we obtain $\delta B_\parallel \sim 0.15$ nT which is quite close to measured value of 0.19 nT (Figure 8c). All estimated values are summarized in Table 3.

For the second event (see Figure 5d, e), a train of electromagnetic EHs with relatively smaller amplitudes ($\delta E_\parallel \pm 50$ mV/m and $\delta B_\parallel \leq 0.05$ nT) is detected before the LHD waves. However, Figure 9 shows (with the same format as Figure 8) a clear electromagnetic EH signature detected around 1001:40.929 UT, about 150 ms before the LHD waves associated with the second DF and 12 s after the LHD waves associated with the first DF. Unipolar $\delta B_\parallel$ up to 0.06 nT (panel c) and bipolar $\delta E_\parallel$ up to ± 90 mV/m (panel f) are measured by MMS3 and MMS4 while only bipolar $\delta E_\parallel$ can be identified on MMS1 and none clear signatures are measured by MMS2. Based on the same analysis as for the first event, we can estimate the EH velocity from the delay between MMS3 and MMS1 signatures as well as from the Lorentz transformation. Considering a delay of 1.55 ms between the center of the bipolar signatures between MMS3 and MMS1, we obtain $v_{EH} \sim 35 \times 10^3$ km/s,

still in the tailward direction and corresponding to $0.94 v_{th,e}$ for $T_e \sim 4$ keV and 0.11c. Then, the parallel length scale is also estimated $\sim$ 77 km as well as the electrostatic potential $V_0 \sim 1.1$ kV and the unipolar component $\delta B_\parallel \sim 0.06$ nT (with $E_\parallel \sim 90$ mV/m, $B_0 = 122$ nT, and $n_0 = 0.05$ p.cm^{-3}). These different results are summarized in Table 3. A last and interesting electromagnetic EH structure is shown on Figure 10. It is detected only by the two satellites MMS3 and MMS4 around 1001:41.399 UT and is superposed to the LHD waves; its properties are also given in Table 3. It is worth noting that MMS3 measures three successive bipolar $\delta E_\parallel$ as well as unipolar $\delta B_\parallel$ with progressively growing amplitudes. The period is about 1.56 ms corresponding to $f \sim 640$ Hz $\sim 0.22 f_{pe} \sim 0.19 f_{ce}$; the time scale of the amplitude growth is $\sim f/3 \sim 0.07 f_{pe}$. This temporal evolution would be consistent with a local instability, a bump-on-tail type, satisfying $\gamma < \omega_r$ (γ being the growth rate and ω_r the real frequency) in a weakly magnetized regime ($f_{ce} \sim f_{pe}$) as investigated by *Umeda et al.* [2004]. Furthermore, as MMS4 only detects the last EH signature (and not the first signatures with smaller amplitudes), it shows that the spatial scale of the EHs grows on this time scale.

6. Discussion

In the present study, we have shown two DF like signatures associated with fast plasma flows and field-aligned current signatures detected during the expansion phase of a large substorm [see also *Nakamura et al.*, 2017]. The first event corresponds to a fast dawnward flow and anti-parallel current which could be associated with a vortex structure generated by the wake of a previous fast earthward plasma flow [*Sergeev et al.*, 2003]. The second event is more classic and corresponds to a fast earthward and duskward plasma flow and a parallel current consistent with a localized substorm current wedge-like signature

("wedgelet") expected to be associated with such a fast earthward flow [*Cao et al.*, 2010; *Liu et al.*, 2013; *Palin et al.*, 2015; *Nakamura et al.*, 2017]. This second event is preceded by a southward/dawnward plasma flow consistent with a brief expansion of the plasma sheet generated by the arrival of the fast earthward/duskward flow. Plasma waves have been displayed in detail for both events.

For the first event, intense electric fluctuations ($\delta E_\perp \sim \pm 200$ mV/m) with frequency close to f_{LH} were detected in association with an ion scale density gradient ($\sim 2d_i$) and propagating dawnward with a phase speed close to the electric drift and the ion thermal velocity. These fluctuations have been identified as LHD waves in section 4. Their amplitudes are larger than those associated with LHD waves ($\sim \pm 50$ mV/m) detected at DF crossed near the equator [*Sergeev et al.*, 2009; *Zhou et al.*, 2009; *Divin et al.*, 2015]; this characteristic is likely related to the present low-β plasma conditions ($\beta_i \sim 0.04$ and $\beta_e \sim 0.01$) as finite β is known to have a stabilizing effect on LHD instability [*Davidson and Gladd*, 1975]. About 0.5 s after the detection of LHD waves, a train of electromagnetic solitary waves with a 1 ms time scale and amplitudes up to $\delta E_\parallel \sim 130$ mV/m and $\delta B_\parallel \sim 0.2$ nT were detected propagating in the tailward direction. They have been identified as electromagnetic electron phase-space holes in section 5.

The second DF event was also accompanied by same types of plasma waves. LHD waves have much smaller amplitudes ($\delta E_\perp \sim \pm 50$ mV/m) and also propagate dawnward with a smaller perpendicular phase speed but still close the electric drift and the ion thermal velocity. A train of electromagnetic EHs is detected with the same polarity as for the first event so still moving tailward. Most of these solitary structures have relatively smaller amplitudes ($\delta E_\parallel \sim \pm 50$ mV/m and $\delta B_\parallel \leq 0.05$ nT) although one

structure reaches $\sim \pm 90$ mV/m and $\delta B_{\parallel} \leq 0.06$ nT) . This train occurs $\sim$ 150 ms before the LHD waves and $\sim$ 12 s after the LHD waves associated with the first DF. Finally, a large amplitude electromagnetic EH ($\delta E_{\parallel} \sim \pm 90$ mV/m) possibly produced by a linearly growing instability is also detected during the LHD wave emission. Note that large amplitude LHD waves associated with electrostatic EHs detected near separatrices during a magnetotail reconnection event have been also reported [*Cattell et al.*, 2005].

To simplify, EH can be generated by two categories of mechanisms: (i) electron-electron beam instabilities with two or more components [e.g., *Omura et al.*, 1996; *Umeda et al.*, 2002, 2004; *Wu et al.*, 2011], and (ii) current-driven like Buneman instabilities [see *Che et al.*, 2010; *Tao et al.*, 2011; *Treumann and Baumjohann*, 2012, and references therein]. The Buneman mode propagates parallel to $\mathbf{B}_0$ with a phase speed $v_B < v_d$ ($v_d = v_i - v_e$ being the ion-electron drift velocity). The fluid-like nature of this instability requires that $v_d > v_{th,e}$ [e. g., *Treumann and Baumjohann*, 2012]. However, we showed that these electromagnetic EHs were propagating towards the tail and would require a strong anti-parallel current (with $v_d > v_{th,e}$) to be driven by the Buneman instability; a current signature which is not measured. Indeed, the anti-parallel current associated with the first event is about -100 nA.m^{-2} which corresponds to $v_d \sim v_{th,i}$ much smaller than $v_{th,e}$. Furthermore, it is also difficult to consider that the measured anti-parallel current results from the initial evolution of the Buneman instability which would have reduced a stronger initial current. Indeed, the electrons which carry the current are moving towards the tail and therefore could not have been produced in a possible tailward reconnection region.

On the other hand, *Cairns and McMillan* [2005]; *Krasnoselskikh et al.* [1985]; *Hsia et al.* [1979] showed that assuming a finite $k_{\parallel} \ll k_{\perp}$, LH waves can accelerate electrons in

the direction parallel to **B**, with the Cherenkov resonant velocity given by $v_{\parallel} = \omega/k_{\parallel} = (m_i/m_e)^{1/2}\omega/k_{\perp}$. Using the value of $\omega/k_{\perp}$ estimated in section 4 for the first event, we obtain the resonant velocity $v_{res} \sim 1.35 v_{th,e}$ corresponding to a resonant energy ~ 6.8 keV, a parallel wavelength ~ 718 km and a wave angle $\sim 88.7°$.

Figure 11a, b shows again for reference the electron density and the LHD electrostatic potential fluctuations associated with the first event and measured by MMS1. The parallel electric field calculated by using the DC-coupled EDP data and the survey magnetic field and its associated error bars as well as the band-pass filtered parallel electric in MFA frame are plotted in Figure 11c, d. Ion differential fluxes parallel, perpendicular and anti-parallel to **B** are shown in Figure 11e-g. Only some energies have been plotted: the magenta line corresponds to the energy channel closest to the resonant energy then we have also selected 7 channels below the resonant energy and all channels above except the last two channels which have been plotted with solid black and brown lines for reference. Also, the two lowest energy channels above the spacecraft potential have been plotted in dotted lines (black and brown). We can see that a sudden increase of the fluxes in the parallel direction occurs for the energy channels around the resonant energy but not for low energies. Therefore this increase could be produced by the wave-particle interaction between these energetic electrons and the LHD waves which have significant parallel electric field component shown in Figure 11c, d. This would also be consistent with sudden increase of the parallel electron temperature shown in figure 6d. Furthermore, the resonant velocity being $1.35 v_{th,e}$, this interaction could be responsible for the generation of parallel electron beams or parallel electron drifts able to destabilize bump-on-tail type or current-driven instabilities (like Buneman) and make the formation of tailward propagating EH possible.

The self-consistent kinetic description of this interaction is out of the scope of this paper. However, we have to point out some puzzling characteristics. As we can see in figure 11e-g, electrons seem to be only accelerated in the direction parallel to **B** while we would expect that the acceleration occurs in both directions. Furthermore, we have noticed in figure 4h that the Poynting vector of the LHD waves changes sign in the middle of the emission; a property that should modify the wave-particle interaction and then the electron acceleration. Finally, figure 6b indicates that the LHD fluctuations are also associated with strong anti-parallel currents which should be taken into account in a full self-consistent kinetic description of the interaction.

McMillan and Cairns [2006] developed such a self-consistent kinetic theory taking into account strong parallel current carried by electrons in the low-β limit in order to apply both the electrostatic and homogeneous plasma approximations. It is interesting to note that assuming a parallel electron drift about $5v_{th,e}$ they found a maximum growth rate for $\omega = 0.9\omega_{LH}$, a quasi-perpendicular propagation with a wave angle $\sim 88.7°$ and a perpendicular phase speed $\omega/k_\perp \sim 3.6v_{th,i}$ (using the center-of-mass frame where ions are at rest) with $k = 0.25\omega_{LH}/v_{th,i}$. Such values are very close to those estimated from our observations ($\omega \sim \omega_{LH}$, quasi-perpendicular propagation) although our estimated phase speed is much smaller $\sim v_{th,i}$ and we have $k = 1.27\omega_{LH}/v_{th,i}$ so a much smaller perpendicular wave length. Furthermore, the measured parallel electron drift, associated with the anti-parallel current, is much smaller $\sim v_{th,i}$ than those assumed by *McMillan and Cairns* [2006].

However, based on 3D electromagnetic PIC simulations in strongly magnetized plasmas ($f_{ce} \gg f_{pe}$), *Che et al.* [2009, 2010] showed that these (quasi-perpendicular) LHD waves

generated by large electron parallel drifts ($> v_{th,e}$) and with a high parallel phase speed are able to generate fast moving electrostatic EHs. On the other hand, in the same strongly magnetized regime and from 2D electrostatic PIC simulations *Miyake et al.* [2000] also pointed out that as the parallel phase speed of EHs can be of the same order of the parallel phase speed of the LHD waves (having a finite $k_{\|}$), EHs can radiate LHD waves by a wave-wave coupling process. Furthermore, a linear kinetic study of the bump-on-tail instability in weakly magnetized regime ($f_{ce} \sim f_{pe}$) showed that electron beam modes have the maximum growth rate ($\gamma \sim 2\pi f_{pe}/10$) for a purely parallel propagation while LHD waves with one order of magnitude smaller growth rate are found at perpendicular propagation [*Umeda et al.*, 2002]. Based on 2D electrostatic as well as electromagnetic PIC simulations, they showed that EHs are generated first by the bump-on-tail mode and then radiate LHD waves later [*Umeda et al.*, 2002, 2004].

In the present observations, LHD waves are observed at large scale by the four satellites (see Figure 6). It does not seem to be consistent with a generation by small scale EHs. On the contrary, we suggest that LHD waves (generated by ion scale density gradients) accelerate electrons in the direction parallel to the magnetic field leading to a bump on the tail of the distribution function near the resonant energy ($\sim 1.35 v_{th,e}$). Then, EHs could be formed via a bump-on-tail type instability or directly by a wave-wave coupling process. Thus, electromagnetic EH signatures shown in Figure10 could be formed by a bump-on-tail type instability satisfying $\gamma \sim 0.07(2\pi f_{pe}) < \omega_r \sim 0.2(2\pi f_{pe})$) as shown by *Umeda et al.* [2004].

Finally, despite of all this evidence regarding LHD wave/EH coupling, we cannot rule out the possibility that the jump of the parallel electron temperature is just caused by

the sudden crossing of a hot plasma associated with the fast dawnward flow and the strong anti-parallel current and not due to a local wave-particle interaction. In such an interpretation LHD waves would be just a by-product of the fast flow propagation and its associated substorm current wedge-like system. Still, the questions related to how these tailward moving electrons are accelerated and how much these LHD waves could participate in the energy dissipation of the flow have to be addressed.

This discussion shows a need to develop a self-consistent kinetic theory of LHD instability for these specific plasma conditions (fast flow i.e. large electric drift v_E, large parallel current i.e. large $v_{d\parallel} = v_{\parallel,i} - v_{\parallel,e}$, together with sharp density gradient i.e. large diamagnetic drift v_{dia} which can or not cancel the electric drift) with both electron-ion parallel and perpendicular drift velocities of the order of the ion thermal velocity. Such a theory would improve our understanding of the source of the LHD waves. Numerical full-particle simulations in weakly magnetized regime ($f_{ce} \sim f_{pe}$) would be also needed to study the non linear regime of this instability and its possible link to the formation of electromagnetic EHs. These developments should be accompanied by detailed investigations based on numerous DF events detected during the current phase 2b of the MMS mission.

7. Conclusions

We reported on MMS observations recorded during the expansion phase of a substorm on August 10th, 2016 while the constellation was located out of the magnetic equator, at the edge of the plasma sheet and in the southern hemisphere. Two DF like signatures associated with fast flows, field-aligned currents and ion scale density gradients were analysed. Ions were found to be decoupled from the magnetic field at the DF due to their diamagnetic drift velocity of the same order of the electric drift. The first event

corresponds to a fast dawnward flow and anti-parallel current which could be related to a vortex-like signature induced by the wake of a previous fast earthward flow. The second event, more classic, corresponds to a fast earthward and duskward flow and a parallel current consistent with a substorm current wedge-like (so called "wedgelet") current system. Yet, it is preceded by a southward/dawnward flow consistent with a brief expansion of the plasma sheet before the DF arrival.

Plasma waves were investigated in detail for both events. Perpendicular electric field fluctuations near the fronts were identified as LHD waves propagating dawnward in a direction quasi-perpendicular to $\mathbf{B}$ with a phase speed close to the electric drift and the ion thermal velocity $v_{th,i}$. Amplitudes and phase speed are larger for the first DF than for the second. Sharp increases of the parallel electron temperature and of the parallel electron fluxes are measured in association with these waves. Electromagnetic EHs propagating tailward along the magnetic field were detected $\sim$ 500 ms after the LHD waves for the first event while for the second event, a train of EHs was identified $\sim$ 150 ms before the LHD waves. Furthermore, a large amplitude electromagnetic EH, preceded by linearly growing oscillations, was detected during the LHD wave emission of the second event. All analysed electromagnetic EH signatures were found to have an internal structure and properties consistent with a cylindrically symmetric potential structure of previous models [*Andersson et al.*, 2009; *Tao et al.*, 2011]. We suggested and showed some evidence that assuming a finite $k_{\parallel}$, LHD waves, generated by ion scale density gradients, could accelerate electrons parallel to $\mathbf{B}$ and generate parallel electron drifts larger than the electron thermal velocity $v_{th,e}$. In a weakly magnetized regime ($f_{ce} \sim f_{pe}$), such large parallel drifts can lead to the formation of electromagnetic EHs by triggering a bump-on-tail instability [*Umeda*

et al., 2004]. Another possibility is that electromagnetic EHs are directly generated by wave-wave coupling with the LHD waves due to the property that the parallel speed phase of LHD waves ($\sim 1.35 v_{th,e}$) is of the same order of the estimated EH parallel speed [*Miyake et al.*, 2000; *Umeda et al.*, 2002]. Furthermore, the fact that the maximum growth rate of LHD waves is for $k_\perp \rho_e \sim 1$ suggests that EHs would be formed with a perpendicular scale equivalent to the electron Larmor radius and then would grow by coalescence in the non linear regime to reach a larger scale as observed [*Umeda et al.*, 2004]. Note that the 30 ms time resolution of the electron distribution functions delivered by FPI is *a priori* not sufficient to follow the EH dynamics (1 ms time scale) and to allows us to distinguish between different formation mechanisms. Thus, the required careful analysis of the electron distribution functions associated with these EHs will be carried out in a future work. Note also that the train of electromagnetic EHs detected before the LHD waves associated with the second DF could be generated by the LHD waves of the first DF. Indeed, in weakly magnetized regime ($f_{ce} \sim f_{pe}$), EHs are not made unstable by electrostatic whistler waves as in strongly magnetized regime [*Goldman et al.*, 1999]. Yet, it would require a quite long stability period of these electromagnetic EHs (~ 12 s $\sim$ a few hundred of thousands of $(2\pi f_{pe})^{-1}$) compared with results obtained by simulations which, so far, have only shown that they can persist for a time longer than several thousands of $(2\pi f_{pe})^{-1}$ [*Umeda et al.*, 2004; *Wu et al.*, 2011].

Finally, the present study cannot rule out the possibility that the parallel electron anisotropy can only be due to the crossing of the field-aligned current system associated with the fast dawnward flow; LHD waves being in such a case a by-product due to field-aligned and/or density gradient free energy sources carried by the fast flow but still able

to participate in the local dissipation process. For such an interpretation, the origin of the accelerated electrons parallel to the magnetic field able to generate EH remains unknown. More theoretical as well as observational investigations are needed to clarify these mechanisms associated with DF structure crossed out of equator. The present MMS phase 2b ("Maha phase") in the magnetotail will provide numerous new DF events which should allow us to shed light on these multiscale kinetic processes.

Acknowledgments. The French involvement (SCM) on MMS is supported by CNES and CNRS. H. B.'s work has been supported by CNES through grant "Allocations de recherche post-doctorale". O. Le Contel thanks the SPEDAS team for their efforts to support the MMS data analysis. All MMS data used are available at https:\\lasp.colorado.edu\mms\sdc\public\about\browse-wrapper\.

This research has made use of NASA's Astrophysics Data System.

References

Andersson, L., R. E. Ergun, J. Tao, A. Roux, O. Lecontel, V. Angelopoulos, J. Bonnell, J. P. McFadden, D. E. Larson, S. Eriksson, T. Johansson, C. M. Cully, D. N. Newman, M. V. Goldman, K.-H. Glassmeier, and W. Baumjohann (2009), New Features of Electron Phase Space Holes Observed by the THEMIS Mission, *Physical Review Letters*, *102*(22), 225004, doi:10.1103/PhysRevLett.102.225004.

Angelopoulos, V., W. Baumjohann, C. F. Kenel, F. V. Coroniti, M. G. Kivelson, R. Pellat, R. J. Walker, H. Lühr, and G. Paschmann (1992), Bursty bulk flows in the inner central plasma sheet, *J. Geophys. Res.*, *97*, 4027.

Angelopoulos, V., J. McFadden, D. Larson, C. Carlson, S. Mende, H. Frey, T. Phan, D. Sibeck, K.-H. Glassmeier, U. Auster, E. Donovan, I. Mann, I. Rae, C. Russell, A. Runov, X. Xhou, and L. Kepko (2008b), Tail reconnection triggering substorm onset, *Science*, doi:10.1126/science.1160495.

Angelopoulos, V., A. Runov, X.-Z. Zhou, D. L. Turner, S. A. Kiehas, S.-S. Li, and I. Shinohara (2013), Electromagnetic Energy Conversion at Reconnection Fronts, *Science*, *341*, 1478–1482, doi:10.1126/science.1236992.

Baker, D. N., T. I. Pulkkinen, V. Angelopoulos, W. Baumjohann, and R. L. McPherron (1996), Neutral line model of substorms: Past results and present view, *J. Geophys. Res.*, *101*, 12,975–13,010, doi:10.1029/95JA03753.

Baumjohann, W., G. Paschmann, and H. L*ü*hr (1990), Characteristics of high-speed ion flows in the plasma sheet, *J. Geophys. Res.*, *95*, 3801.

Birn, J., and M. Hesse (1991), The substorm current wedge and field-aligned currents in MHD simulations of magnetotail reconnection, *J. Geophys. Res.*, *96*, 1611–1618, doi:10.1029/90JA01762.

Birn, J., and M. Hesse (2005), Energy release and conversion by reconnection in the magnetotail, *Annales Geophysicae*, *23*, 3365–3373, doi:10.5194/angeo-23-3365-2005.

Blake, J. B., B. H. Mauk, D. N. Baker, P. Carranza, J. H. Clemmons, J. Craft, W. R. Crain, A. Crew, Y. Dotan, J. F. Fennell, R. H. Friedel, L. M. Friesen, F. Fuentes, R. Galvan, C. Ibscher, A. Jaynes, N. Katz, M. Lalic, A. Y. Lin, D. M. Mabry, T. Nguyen, C. Pancratz, M. Redding, G. D. Reeves, S. Smith, H. E. Spence, and J. Westlake (2016), The Fly's Eye Energetic Particle Spectrometer (FEEPS) Sensors for the Magnetospheric Multiscale (MMS) Mission, *Space Science Rev.*, *199*, 309–329, doi:10.1007/s11214-015-

0163-x.

Breuillard, H., O. Le Contel, A. Retino, A. Chasapis, T. Chust, L. Mirioni, D. B. Graham, F. D. Wilder, I. Cohen, A. Vaivads, Y. V. Khotyaintsev, P.-A. Lindqvist, G. T. Marklund, J. L. Burch, R. B. Torbert, R. E. Ergun, K. A. Goodrich, J. Macri, J. Needell, M. Chutter, D. Rau, I. Dors, C. T. Russell, W. Magnes, R. J. Strangeway, K. R. Bromund, F. Plaschke, D. Fischer, H. K. Leinweber, B. J. Anderson, G. Le, J. A. Slavin, E. L. Kepko, W. Baumjohann, B. Mauk, S. A. Fuselier, and R. Nakamura (2016), Multispacecraft analysis of dipolarization fronts and associated whistler wave emissions using MMS data, *Geophys. Res. Lett.*, *43*, 7279–7286, doi:10.1002/2016GL069188.

Burch, J. L., R. B. Torbert, T. D. Phan, L.-J. Chen, T. E. Moore, R. D. Ergun, J. P. Eastwood, D. J. Gershman, P. A. Cassak, M. R. Argall, S. Wang, M. Hesse, C. J. Pollock, B. L. Giles, R. Nakamura, B. H. Mauk, S. A. Fuselier, C. T. Russell, R. J. Strangeway, J. F. Drake, M. A. Shay, Y. V. Khotyaintsev, G. Lindqvist, P.-A.and Marklund, F. D. Wilder, D. T. Young, K. Torkar, J. Goldstein, J. C. Dorelli, L. A. Avanov, M. Oka, D. N. Baker, A. N. Jaynes, K. A. Goodrich, I. J. Cohen, D. L. Turner, J. F. Fennell, J. B. Blake, J. Clemmons, M. Goldman, D. Newman, S. M. Petrinec, K. J. Trattner, B. Lavraud, P. H. Reiff, W. Baumjohann, W. Magnes, M. Steller, W. Lewis, Y. Saito, V. Coffey, and M. Chandler (2016), Electron-Scale Measurements of Magnetic Reconnection in Space, *Science*, doi:doi:10.1126/science.aaf2939.

Cairns, I. H., and B. F. McMillan (2005), Electron acceleration by lower hybrid waves in magnetic reconnection regions, *Physics of Plasmas*, *12*(10), 102110, doi:10.1063/1.2080567.

Cao, J.-B., C. Yan, M. Dunlop, H. Reme, I. Dandouras, T. Zhang, D. Yang, A. Moiseyev, S. I. Solovyev, Z. Q. Wang, A. Leonoviche, N. Zolotukhina, and V. Mishin (2010), Geomagnetic signatures of current wedge produced by fast flows in a plasma sheet, *Journal of Geophysical Research (Space Physics)*, *115*, A08205, doi:10.1029/2009JA014891.

Cattell, C., J. Dombeck, J. Wygant, J. F. Drake, M. Swisdak, M. L. Goldstein, W. Keith, A. Fazakerley, M. André, E. Lucek, and A. Balogh (2005), Cluster observations of electron holes in association with magnetotail reconnection and comparison to simulations, *Journal of Geophysical Research (Space Physics)*, *110*, A01211, doi: 10.1029/2004JA010519.

Che, H., J. F. Drake, M. Swisdak, and P. H. Yoon (2009), Nonlinear Development of Streaming Instabilities in Strongly Magnetized Plasma, *Physical Review Letters*, *102*(14), 145004, doi:10.1103/PhysRevLett.102.145004.

Che, H., J. F. Drake, M. Swisdak, and P. H. Yoon (2010), Electron holes and heating in the reconnection dissipation region, *Geophys. Res. Lett.*, *37*, L11105, doi: 10.1029/2010GL043608.

Davidson, R. C., and N. T. Gladd (1975), Anomalous transport properties associated with the lower-hybrid-drift instability, *Physics of Fluids*, *18*, 1327–1335, doi: 10.1063/1.861021.

Deng, X., M. Ashour-Abdalla, M. Zhou, R. Walker, M. El-Alaoui, V. Angelopoulos, R. E. Ergun, and D. Schriver (2010), Wave and particle characteristics of earthward electron injections associated with dipolarization fronts, *Journal of Geophysical Research (Space Physics)*, *115*, A09225, doi:10.1029/2009JA015107.

Divin, A., Y. V. Khotyaintsev, A. Vaivads, and M. André (2015), Lower hybrid drift instability at a dipolarization front, *Journal of Geophysical Research (Space Physics)*.

Ergun, R. E., C. W. Carlson, J. P. McFadden, F. S. Mozer, G. T. Delory, W. Peria, C. C. Chaston, M. Temerin, R. Elphic, R. Strangeway, R. Pfaff, C. A. Cattell, D. Klumpar, E. Shelley, W. Peterson, E. Moebius, and L. Kistler (1998), FAST satellite wave observations in the AKR source region, *Geophys. Res. Lett.*, *25*, 2061–2064, doi:10.1029/98GL00570.

Ergun, R. E., S. Tucker, J. Westfall, K. A. Goodrich, D. M. Malaspina, D. Summers, J. Wallace, M. Karlsson, J. Mack, N. Brennan, B. Pyke, P. Withnell, R. Torbert, J. Macri, D. Rau, I. Dors, J. Needell, P.-A. Lindqvist, G. Olsson, and C. M. Cully (2016), The Axial Double Probe and Fields Signal Processing for the MMS Mission, *Space Sci. Rev.*, *199*, 167–188, doi:10.1007/s11214-014-0115-x.

Fischer, D., W. Magnes, C. Hagen, I. Dors, M. W. Chutter, J. Needell, R. B. Torbert, O. Le Contel, R. J. Strangeway, G. Kubin, A. Valavanoglou, F. Plaschke, R. Nakamura, L. Mirioni, C. T. Russell, H. K. Leinweber, K. R. Bromund, G. Le, L. Kepko, B. J. Anderson, J. A. Slavin, and W. Baumjohann (2016), Optimized merging of search coil and fluxgate data for MMS, *Geoscientific Instrumentation, Methods and Data Systems*, *5*, 521–530, doi:10.5194/gi-5-521-2016.

Fu, H. S., Y. V. Khotyaintsev, A. Vaivads, M. André, and S. Y. Huang (2012), Electric structure of dipolarization front at sub-proton scale, *Geophys. Res. Lett.*, *39*, L06105, doi:10.1029/2012GL051274.

Gershman, D. J., J. C. Dorelli, A. F.-Viñas, and C. J. Pollock (2015), The calculation of moment uncertainties from velocity distribution functions with random errors, *Journal*

of Geophysical Research (Space Physics), *120*, 6633–6645, doi:10.1002/2014JA020775.

Goldman, M. V., M. M. Oppenheim, and D. L. Newman (1999), Nonlinear two-stream instabilities as an explanation for auroral bipolar wave structures, *Geophys. Res. Lett.*, *26*, 1821–1824, doi:10.1029/1999GL900435.

Hsia, J. B., S. M. Chiu, M. F. Hsia, R. L. Chou, and C. S. Wu (1979), Generalized lower-hybrid-drift instability, *Physics of Fluids*, *22*, 1737–1746, doi:10.1063/1.862810.

Huba, J. D., N. T. Gladd, and K. Papadopoulos (1978), Lower-hybrid-drift wave turbulence in the distant magnetotail, *J. Geophys. Res.*, *83*, 5217–5226, doi:10.1029/JA083iA11p05217.

Kennel, C. F. (1995), *Convection and Substorms*, Oxford Univ. Press, New York.

Khotyaintsev, Y. V., A. Vaivads, M. André, M. Fujimoto, A. Retinò, and C. J. Owen (2010), Observations of Slow Electron Holes at a Magnetic Reconnection Site, *Physical Review Letters*, *105*(16), 165002, doi:10.1103/PhysRevLett.105.165002.

Khotyaintsev, Y. V., C. M. Cully, A. Vaivads, M. André, and C. J. Owen (2011), Plasma Jet Braking: Energy Dissipation and Nonadiabatic Electrons, *Physical Review Letters*, *106*(16), 165001, doi:10.1103/PhysRevLett.106.165001.

Kojima, H., H. Matsumoto, T. Miyatake, I. Nagano, A. Fujita, L. A. Frank, T. Mukai, W. R. Paterson, Y. Saito, and S. Machida (1994), Relation between electrostatic solitary waves and hot plasma flow in the plasma sheet boundary layer: GEOTAIL observations, *Geophys. Res. Lett.*, *21*, 2919–2922, doi:10.1029/94GL02111.

Krasnoselskikh, V. V., E. N. Kruchina, A. S. Volokitin, and G. Thejappa (1985), Fast electron generation in quasiperpendicular shocks and type II solar radiobursts, *Astron. Astrophys.*, *149*, 323–329.

Le Contel, O., P. Leroy, A. Roux, C. Coillot, D. Alison, A. Bouabdellah, L. Mirioni, L. Meslier, A. Galic, M. C. Vassal, R. B. Torbert, J. Needell, D. Rau, I. Dors, R. E. Ergun, J. Westfall, D. Summers, J. Wallace, W. Magnes, A. Valavanoglou, G. Olsson, M. Chutter, J. Macri, S. Myers, S. Turco, J. Nolin, D. Bodet, K. Rowe, M. Tanguy, and B. de la Porte (2016), The Search-Coil Magnetometer for MMS, *Space Science Rev.*, *199*, 257–282, doi:10.1007/s11214-014-0096-9.

Lindqvist, P.-A., G. Olsson, R. B. Torbert, B. King, M. Granoff, D. Rau, G. Needell, S. Turco, I. Dors, P. Beckman, J. Macri, C. Frost, J. Salwen, A. Eriksson, L. Åhlén, Y. V. Khotyaintsev, J. Porter, K. Lappalainen, R. E. Ergun, W. Wermeer, and S. Tucker (2016), The Spin-Plane Double Probe Electric Field Instrument for MMS, *Space Sci. Rev.*, *199*, 137–165, doi:10.1007/s11214-014-0116-9.

Liu, J., V. Angelopoulos, A. Runov, and X.-Z. Zhou (2013), On the current sheets surrounding dipolarizing flux bundles in the magnetotail: The case for wedgelets, *Journal of Geophysical Research (Space Physics)*, *118*, 2000–2020, doi:10.1002/jgra.50092.

Liu, W. W., J. Liang, E. F. Donovan, and E. Spanswick (2012), If substorm onset triggers tail reconnection, what triggers substorm onset?, *Journal of Geophysical Research (Space Physics)*, *117*, A11220, doi:10.1029/2012JA018161.

Lui, A. T. Y., C.-L. Chang, A. Mankofsky, H.-K. Wong, and D. Winske (1991), A cross-field current instability for substorm expansions, *J. Geophys. Res.*, *96*, 11,389–11,401.

Lui, A. T. Y., V. Angelopoulos, S. B. Mende, O. Le Contel, H. Frey, E. Donovan, D. G. Sibeck, W. Liu, H. U. Auster, D. Larson, X. Li, M. Nose, and M. O. Fillingim (2008), Determination of the substorm initiation region from a major conjunction interval of themis satellites, *J. Geophys. Res.*, in press.

Mauk, B. H., J. B. Blake, D. N. Baker, J. H. Clemmons, G. D. Reeves, H. E. Spence, S. E. Jaskulek, C. E. Schlemm, L. E. Brown, S. A. Cooper, J. V. Craft, J. F. Fennell, R. S. Gurnee, C. M. Hammock, J. R. Hayes, P. A. Hill, G. C. Ho, J. C. Hutcheson, A. D. Jacques, S. Kerem, D. G. Mitchell, K. S. Nelson, N. P. Paschalidis, E. Rossano, M. R. Stokes, and J. H. Westlake (2016), The Energetic Particle Detector (EPD) Investigation and the Energetic Ion Spectrometer (EIS) for the Magnetospheric Multiscale (MMS) Mission, *Space Science Rev.*, *199*, 471–514, doi:10.1007/s11214-014-0055-5.

McMillan, B. F., and I. H. Cairns (2006), Lower hybrid turbulence driven by parallel currents and associated electron energization, *Physics of Plasmas*, *13*(5), 052104, doi: 10.1063/1.2198212.

McPherron, R. L., C. T. Russell, and M. P. Aubry (1973), Satellite studies of magnetospheric substorms on August 15, 1968: 9. Phenomenological model for substorms, *J. Geophys. Res.*, *78*, 3131, doi:10.1029/JA078i016p03131.

Miyake, T., Y. Omura, and H. Matsumoto (2000), Electrostatic particle simulations of solitary waves in the auroral region, *J. Geophys. Res.*, *105*, 23,239–23,250, doi: 10.1029/2000JA000001.

Nakamura, M. S., H. Matsumoto, and M. Fujimoto (2002), Interchange instability at the leading part of reconnection jets, *Geophys. Res. Lett.*, *29*, 1247, doi: 10.1029/2001GL013780.

Nakamura, R., T. Nagai, J. Birn, V. A. Sergeev, O. Le Contel, A. Varsani, W. Baumjohann, T. Nakamura, A. Artemyev, R. E. Ergun, S. A. Fuselier, D. J. Gershman, B. J. Giles, Yu. V. Khotyaintsev, P.-A. Lindqvist, W. Magnes, B. Mauk, C. T. Russell, H. J. Singer, J. Stawarz, R. J. Strangeway, B. Anderson, K. R. Bromund, D. Fischer,

L. Kepko, G. Le, F. Plaschke, J. A. Slavin, I. Cohen, A. Jaynes, and D. L. Turner (2017), Near-earth plasma sheet boundary dynamics during substorm dipolarization, *Earth, Planets Space*, doi:10.1186/s40623-017-0707-2.

Norgren, C., A. Vaivads, Y. V. Khotyaintsev, and M. André (2012), Lower Hybrid Drift Waves: Space Observations, *Physical Review Letters*, *109*(5), 055001, doi: 10.1103/PhysRevLett.109.055001.

Ohtani, S.-I., M. A. Shay, and T. Mukai (2004), Temporal structure of the fast convective flow in the plasma sheet: Comparison between observations and two-fluid simulations, *Journal of Geophysical Research (Space Physics)*, *109*, A03210, doi: 10.1029/2003JA010002.

Omura, Y., H. Matsumoto, T. Miyake, and H. Kojima (1996), Electron beam instabilities as generation mechanism of electrostatic solitary waves in the magnetotail, *J. Geophys. Res.*, *101*, 2685–2698, doi:10.1029/95JA03145.

Palin, L., C. Jacquey, H. Opgenoorth, M. Connors, V. Sergeev, J.-A. Sauvaud, R. Nakamura, G. D. Reeves, H. J. Singer, V. Angelopoulos, and L. Turc (2015), Three-dimensional current systems and ionospheric effects associated with small dipolarization fronts, *Journal of Geophysical Research (Space Physics)*, *120*, 3739–3757, doi: 10.1002/2015JA021040.

Pollock, C., T. Moore, A. Jacques, J. Burch, U. Gliese, Y. Saito, T. Omoto, L. Avanov, A. Barrie, V. Coffey, J. Dorelli, D. Gershman, B. Giles, T. Rosnack, C. Salo, S. Yokota, M. Adrian, C. Aoustin, C. Auletti, S. Aung, V. Bigio, N. Cao, M. Chandler, D. Chornay, K. Christian, G. Clark, G. Collinson, T. Corris, A. De Los Santos, R. Devlin, T. Diaz, T. Dickerson, C. Dickson, A. Diekmann, F. Diggs, C. Duncan, A. Figueroa-Vinas,

C. Firman, M. Freeman, N. Galassi, K. Garcia, G. Goodhart, D. Guererro, J. Hageman, J. Hanley, E. Hemminger, M. Holland, M. Hutchins, T. James, W. Jones, S. Kreisler, J. Kujawski, V. Lavu, J. Lobell, E. LeCompte, A. Lukemire, E. MacDonald, A. Mariano, T. Mukai, K. Narayanan, Q. Nguyan, M. Onizuka, W. Paterson, S. Persyn, B. Piepgrass, F. Cheney, A. Rager, T. Raghuram, A. Ramil, L. Reichenthal, H. Rodriguez, J. Rouzaud, A. Rucker, Y. Saito, M. Samara, J.-A. Sauvaud, D. Schuster, M. Shappirio, K. Shelton, D. Sher, D. Smith, K. Smith, S. Smith, D. Steinfeld, R. Szymkiewicz, K. Tanimoto, J. Taylor, C. Tucker, K. Tull, A. Uhl, J. Vloet, P. Walpole, S. Weidner, D. White, G. Winkert, P.-S. Yeh, and M. Zeuch (2016), Fast Plasma Investigation for Magnetospheric Multiscale, *Space Science Rev.*, *199*, 331–406, doi:10.1007/s11214-016-0245-4.

Pritchett, P. L., and R. J. Strangeway (1985), A simulation study of kilometric radiation generation along an auroral field line, *J. Geophys. Res.*, *90*, 9650–9662, doi:10.1029/JA090iA10p09650.

Pritchett, P. L., F. V. Coroniti, and Y. Nishimura (2014), The kinetic ballooning/interchange instability as a source of dipolarization fronts and auroral streamers, *Journal of Geophysical Research (Space Physics)*, *119*, 4723–4739, doi:10.1002/2014JA019890.

Roux, A., S. Perraut, P. Robert, A. Morane, A. Pedersen, A. Korth, G. Kremser, B. Aparicio, D. Rodgers, and R. Pellinen (1991), Plasma sheet instability related to the westward traveling surge, *J. Geophys. Res.*, *96*, 17,697.

Runov, A., V. Angelopoulos, M. I. Sitnov, V. A. Sergeev, J. Bonnell, J. P. McFadden, D. Larson, K.-H. Glassmeier, and U. Auster (2009), THEMIS observations of

an earthward-propagating dipolarization front, *Geophys. Res. Lett.*, *36*, L14106, doi: 10.1029/2009GL038980.

Russell, C. T., B. J. Anderson, W. Baumjohann, K. R. Bromund, D. Dearborn, D. Fischer, G. Le, H. K. Leinweber, D. Leneman, W. Magnes, J. D. Means, M. B. Moldwin, R. Nakamura, D. Pierce, F. Plaschke, K. M. Rowe, J. A. Slavin, R. J. Strangeway, R. Torbert, C. Hagen, I. Jernej, A. Valavanoglou, and I. Richter (2016), The Magnetospheric Multiscale Magnetometers, *Space Sci. Rev.*, *199*, 189–256, doi:10.1007/s11214-014-0057-3.

Schmid, D., M. Volwerk, R. Nakamura, W. Baumjohann, and M. Heyn (2011), A statistical and event study of magnetotail dipolarization fronts, *Annales Geophysicae*, *29*, 1537–1547, doi:10.5194/angeo-29-1537-2011.

Scholer, M., and A. Otto (1991), Magnetotail reconnection - Current diversion and field-aligned currents, *Geophys. Res. Lett.*, *18*, 733–736, doi:10.1029/91GL00361.

Sergeev, V., A. Runov, W. Baumjohann, R. Nakamura, T. L. Zhang, M. Volwerk, A. Balogh, H. Rème, J. A. Sauvaud, M. André, and B. Klecker (2003), Current sheet flapping motion and structure observed by Cluster, *Geophys. Res. Lett.*, *30*, 1327, doi: 10.1029/2002GL016500.

Sergeev, V., V. Angelopoulos, S. Apatenkov, J. Bonnell, R. Ergun, R. Nakamura, J. McFadden, D. Larson, and A. Runov (2009), Kinetic structure of the sharp injection/dipolarization front in the flow-braking region, *Geophys. Res. Lett.*, *36*, L21105, doi:10.1029/2009GL040658.

Sitnov, M. I., M. Swisdak, and A. V. Divin (2009), Dipolarization fronts as a signature of transient reconnection in the magnetotail, *Journal of Geophysical Research (Space Physics)*, *114*, A04202, doi:10.1029/2008JA013980.

Strangeway, R. J., L. Kepko, R. C. Elphic, C. W. Carlson, R. E. Ergun, J. P. McFadden, W. J. Peria, G. T. Delory, C. C. Chaston, M. Temerin, C. A. Cattell, E. Möbius, L. M. Kistler, D. M. Klumpar, W. K. Peterson, E. G. Shelley, and R. F. Pfaff (1998), FAST observations of VLF waves in the auroral zone: Evidence of very low plasma densities, *Geophys. Res. Lett.*, *25*, 2065–2068, doi:10.1029/98GL00664.

Tao, J. B., R. E. Ergun, L. Andersson, J. W. Bonnell, A. Roux, O. LeContel, V. Angelopoulos, J. P. McFadden, D. E. Larson, C. M. Cully, H.-U. Auster, K.-H. Glassmeier, W. Baumjohann, D. L. Newman, and M. V. Goldman (2011), A model of electromagnetic electron phase-space holes and its application, *Journal of Geophysical Research (Space Physics)*, *116*, A11213, doi:10.1029/2010JA016054.

Torbert, R. B., C. T. Russell, W. Magnes, R. E. Ergun, P.-A. Lindqvist, O. LeContel, H. Vaith, J. Macri, S. Myers, D. Rau, J. Needell, B. King, M. Granoff, M. Chutter, I. Dors, G. Olsson, Y. V. Khotyaintsev, A. Eriksson, C. A. Kletzing, S. Bounds, B. Anderson, W. Baumjohann, M. Steller, K. Bromund, G. Le, R. Nakamura, R. J. Strangeway, H. K. Leinweber, S. Tucker, J. Westfall, D. Fischer, F. Plaschke, J. Porter, and K. Lappalainen (2016), The FIELDS Instrument Suite on MMS: Scientific Objectives, Measurements, and Data Products, *Space Sci. Rev.*, *199*, 105–135, doi:10.1007/s11214-014-0109-8.

Treumann, R. A., and W. Baumjohann (2012), Magnetic field amplification in electron phase-space holes and related effects, *Annales Geophysicae*, *30*, 711–724, doi:10.5194/angeo-30-711-2012.

Umeda, T., Y. Omura, H. Matsumoto, and H. Usui (2002), Formation of electrostatic solitary waves in space plasmas: Particle simulations with open boundary conditions,

Journal of Geophysical Research (Space Physics), *107*, 1449, doi:10.1029/2001JA000286.

Umeda, T., Y. Omura, and H. Matsumoto (2004), Two-dimensional particle simulation of electromagnetic field signature associated with electrostatic solitary waves, *Journal of Geophysical Research (Space Physics)*, *109*, A02207, doi:10.1029/2003JA010000.

Viberg, H., Y. V. Khotyaintsev, A. Vaivads, M. André, H. S. Fu, and N. Cornilleau-Wehrlin (2014), Whistler mode waves at magnetotail dipolarization fronts, *Journal of Geophysical Research (Space Physics)*, *119*, 2605–2611, doi:10.1002/2014JA019892.

Wang, R., Q. Lu, Y. V. Khotyaintsev, M. Volwerk, A. Du, R. Nakamura, W. D. Gonzalez, X. Sun, W. Baumjohann, X. Li, T. Zhang, A. N. Fazakerley, C. Huang, and M. Wu (2014), Observation of double layer in the separatrix region during magnetic reconnection, *Geophys. Res. Lett.*, *41*, 4851–4858, doi:10.1002/2014GL061157.

Wu, M., Q. Lu, A. Du, J. Xie, and S. Wang (2011), The evolution of the magnetic structures in electron phase-space holes: Two-dimensional particle-in-cell simulations, *Journal of Geophysical Research (Space Physics)*, *116*, A10208, doi:10.1029/2011JA016486.

Young, D. T., J. L. Burch, R. G. Gomez, A. De Los Santos, G. P. Miller, P. Wilson, N. Paschalidis, S. A. Fuselier, K. Pickens, E. Hertzberg, C. J. Pollock, J. Scherrer, P. B. Wood, E. T. Donald, D. Aaron, J. Furman, D. George, R. S. Gurnee, R. S. Hourani, A. Jacques, T. Johnson, T. Orr, K. S. Pan, S. Persyn, S. Pope, J. Roberts, M. R. Stokes, K. J. Trattner, and J. M. Webster (2016), Hot Plasma Composition Analyzer for the Magnetospheric Multiscale Mission, *Space Science Rev.*, *199*, 407–470, doi:10.1007/s11214-014-0119-6.

Zhou, M., M. Ashour-Abdalla, X. Deng, D. Schriver, M. El-Alaoui, and Y. Pang (2009), THEMIS observation of multiple dipolarization fronts and associated wave

characteristics in the near-Earth magnetotail, *Geophys. Res. Lett.*, *36*, L20107, doi: 10.1029/2009GL040663.

Table 1. Properties of the electrostatic potential fluctuations for event 1 between 1001:27.850 and 100128.250 UT

satellite	f (Hz)	f_{LH} (Hz)	$v_{\perp,ph}$ (km/s) in GSE	$\lambda_\perp$ (km)	$k_\perp\rho_e$	$\delta\phi/T_e$	Cor. rate
MMS1	64.0	54.9	1147.1×[-0.051,-0.998, -0.032]	17.9	0.50	0.22	0.96
MMS2	54.6	54.8	1091.3×[-0.010,-0.998,-0.046]	20.0	0.44	0.25	0.94
MMS3	64.1	55.8	1217.6×[0.029,-0.996,0.084]	19.0	0.48	0.23	0.93
MMS4	68.3	55.6	1144.9×[0.039,-0.992,0.118]	16.8	0.54	0.36	0.96

Table 2. Properties of the electrostatic potential fluctuations for event 2 between 1001:41.200 and 100141.500 UT for all spacecraft but MMS3 between 1001:41.150 and 1001:41.300 UT.

satellite	f (Hz)	f_{LH} (Hz)	$v_{\perp,ph}$ (km/s) in GSE	$\lambda_\perp$ (km)	$k_\perp\rho_e$	$\delta\phi/T_e$	Cor. Rate
MMS1	68.3	60.0	551.6×[0.068,-0.972,0.219]	8.1	1.33	0.05	0.61
MMS2	45.0	59.7	491.4×[-0.254,-0.889,-0.378]	10.9	0.96	0.04	0.72
MMS3	46.5	60.2	682.9×[-0.193,-0.944,-0.265]	14.7	0.73	0.05	0.66
MMS4	59.4	60.5	770.4×[-0.024,-0.997,0.053]	13.0	0.83	0.06	0.63

Table 3. Properties of the electromagnetic electron phase-space holes associated with the first and second DF. EH velocities ($v_{EH} = -c^2\delta B_x/\delta E_y = c^2\delta B_y/\delta E_x$) and parallel length scales are given in 10^3 km/s and km respectively. Potential V_0 is given in kV and $\delta B_\parallel$ in nT.

Time	$-c^2\delta B_x/\delta E_y$	$c^2\delta B_y/\delta E_x$	$v_{EH,31}$	$v_{EH}/v_{th,e}$	v_{EH}/c	$L_\parallel$	V_0	$\delta B_{\parallel,meas}$	$\delta B_{\parallel,calc}$
1001:28.566	67.5	100.0	45-55	1.2-1.8	0.15-0.22	45-60	1.1	0.19	0.15
1001:40.929	25.7	27.0	35	0.7-0.94	0.09-0.11	58-77	1.1	0.06	0.06
1001:41.399	112.5	56.2	?	1.5	0.19	88	1.3	0.10	0.15

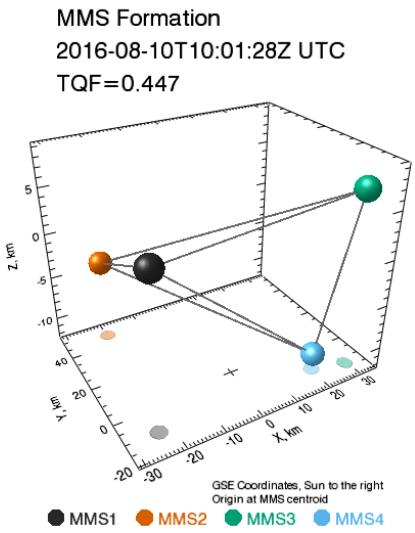

Figure 1. MMS configuration.

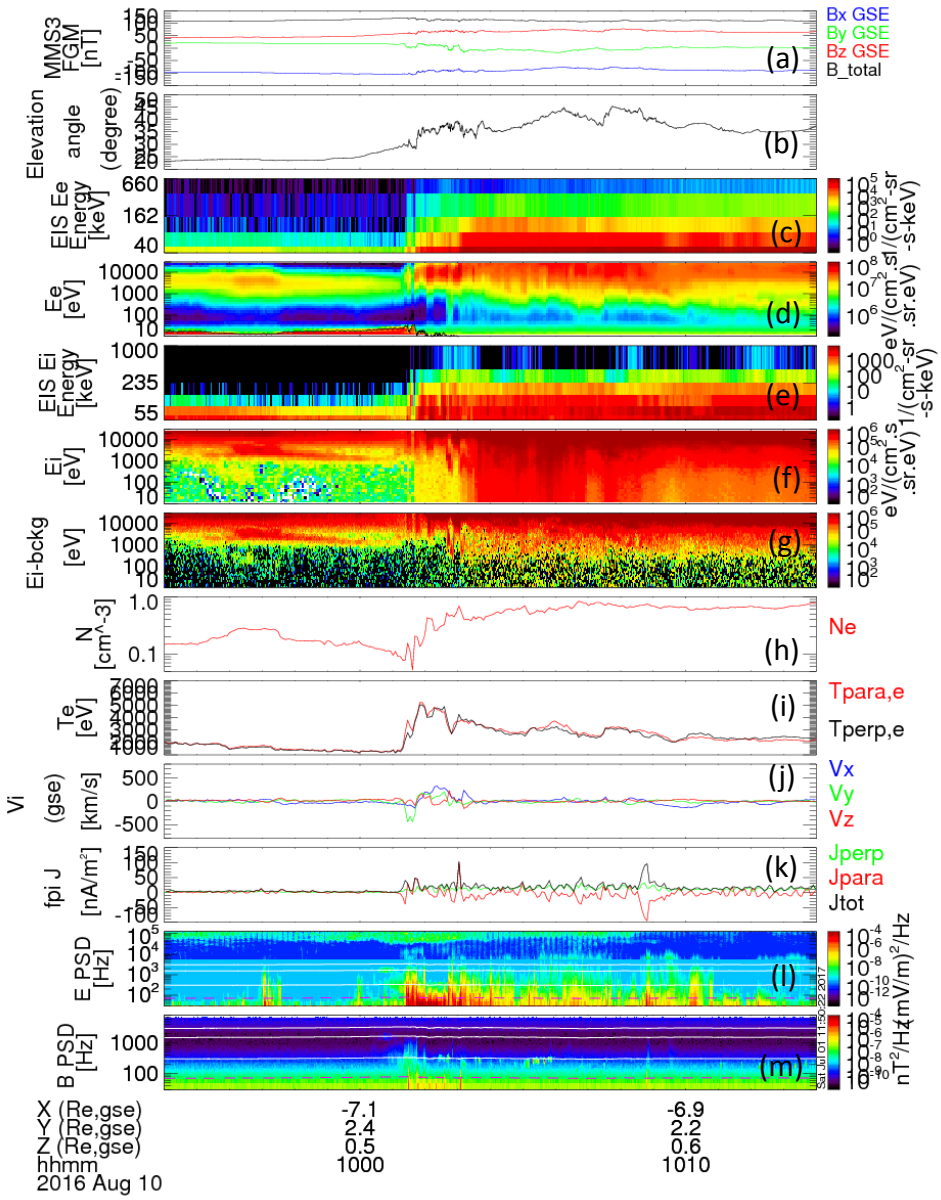

Figure 2. Overview of MMS3 observations on August 10, 2016 between 0950 and 1015 UT.(a) Three components and magnitude of the magnetic field, (b) elevation angle, (c,d) energetic (EIS) and thermal (FPI) electron energy spectrograms (superposed black line corresponds to the spacecraft potential below which photo–electrons are detected), (e,f) energetic (EIS) and thermal (FPI) ion energy spectrograms, (g) thermal (FPI) ion energy spectrograms after subtracting background noise, (h) electron density,(i) parallel (red) and perpendicular (black) electron temperatures, (j) three components of the bulk velocity,(k) parallel (red), perpendicular (green) and total (black) currents, (l,m) electric and magnetic field power spectral densities. White lines indicate f_{ce} the electron gyrofrequency, $f_{ce}/2$ and $f_{ce}/10$. Dashed line indicates the lower-hybrid frequency $\sim \sqrt{f_{ce} f_{ci}}$.

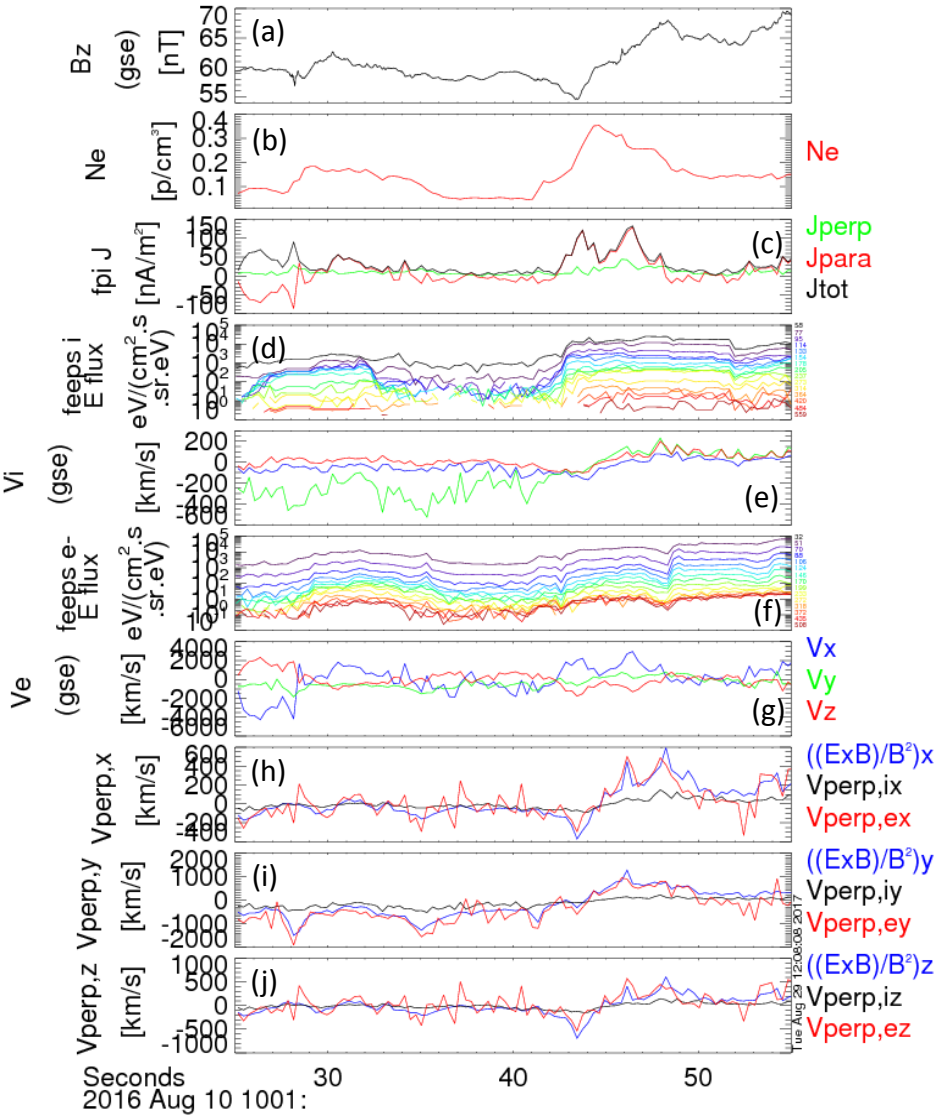

Figure 3. First two dipolarization-like signatures detected by MMS4 between 1001:25 and 1001:55 UT. (a) B_z component in GSE, (b) electron density, (c) 300 ms time-averaged parallel (red), perpendicular (green) and total (black) currents, (d) energetic ion differential fluxes from FEEPS for selected keV energies [58,77,95,114, 133,154,178,205,237,273,314,364,420,484,559] (e) 300 ms time-averaged ion bulk velocities, (f) energetic electron differential fluxes from FEEPS for selected keV energies [32,51,70,88,106,124,146,170,199,233,272,318,372,435,508], (g) 300 ms time-averaged electron bulk velocities (h-j) comparison along x, y and z between 300 ms time-averaged $(\mathbf{E} \times \mathbf{B})/B^2$, ion and electron perpendicular velocities.

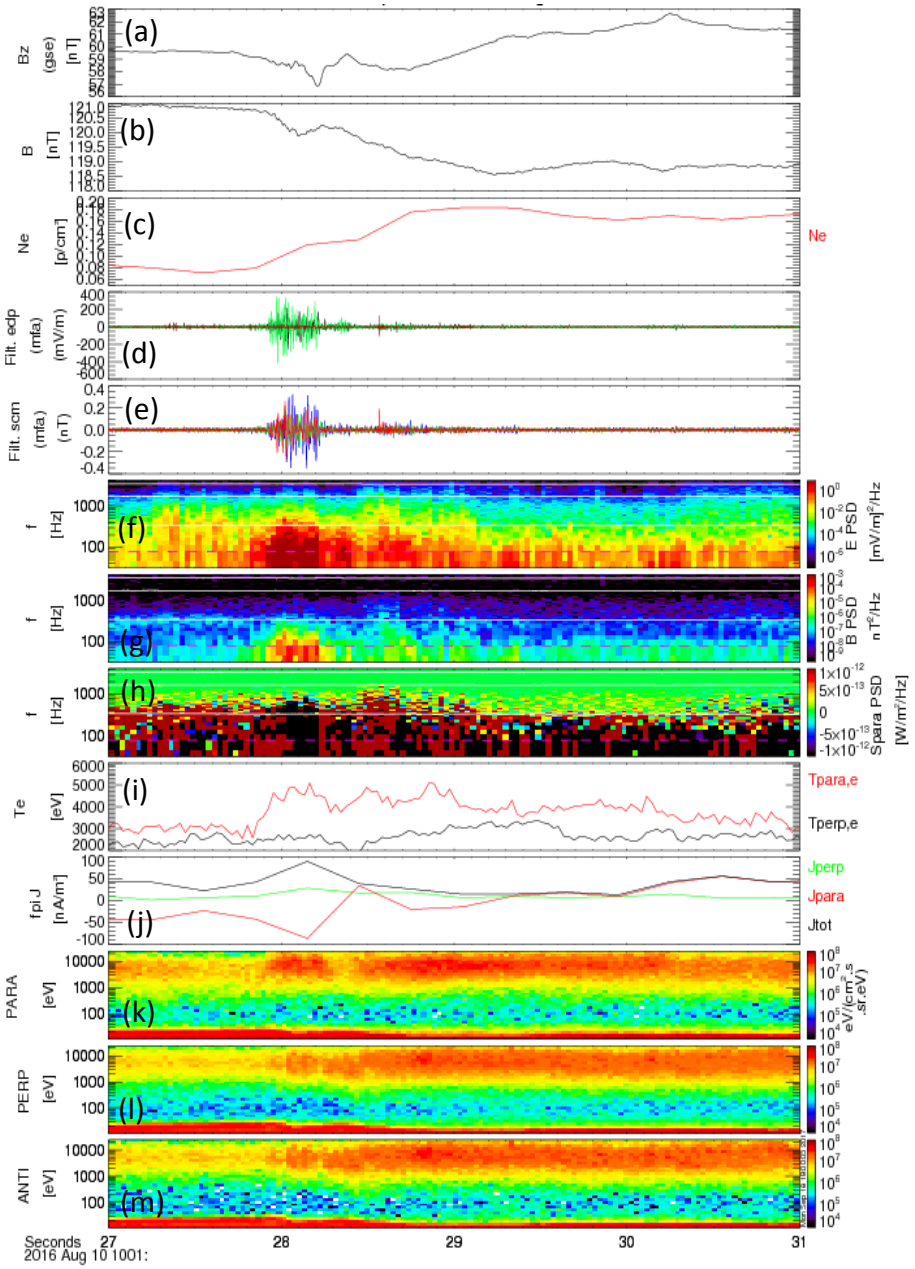

Figure 4. First dipolarization front like signature detected by MMS4 between 1001:27.0 and 100131.0 UT.(a) B_z component in GSE, (b) magnitude of **B**, (c) electron density, (d,e) electric and magnetic waveforms in a magnetic-field aligned coordinate band-pass filtered between 32 Hz and 4 kHz (black and green lines are perpendicular components, red is parallel component), (f,e) omni-directional electric and magnetic power spectral densities,(h) parallel to **B** component of the Poynting vector, (i) parallel (red) and perpendicular (black) electron temperatures, (j) parallel (red), perpendicular (green) and total (black) currents, (k-m) parallel, perpendicular and anti-parallel energy spectrograms of electrons.

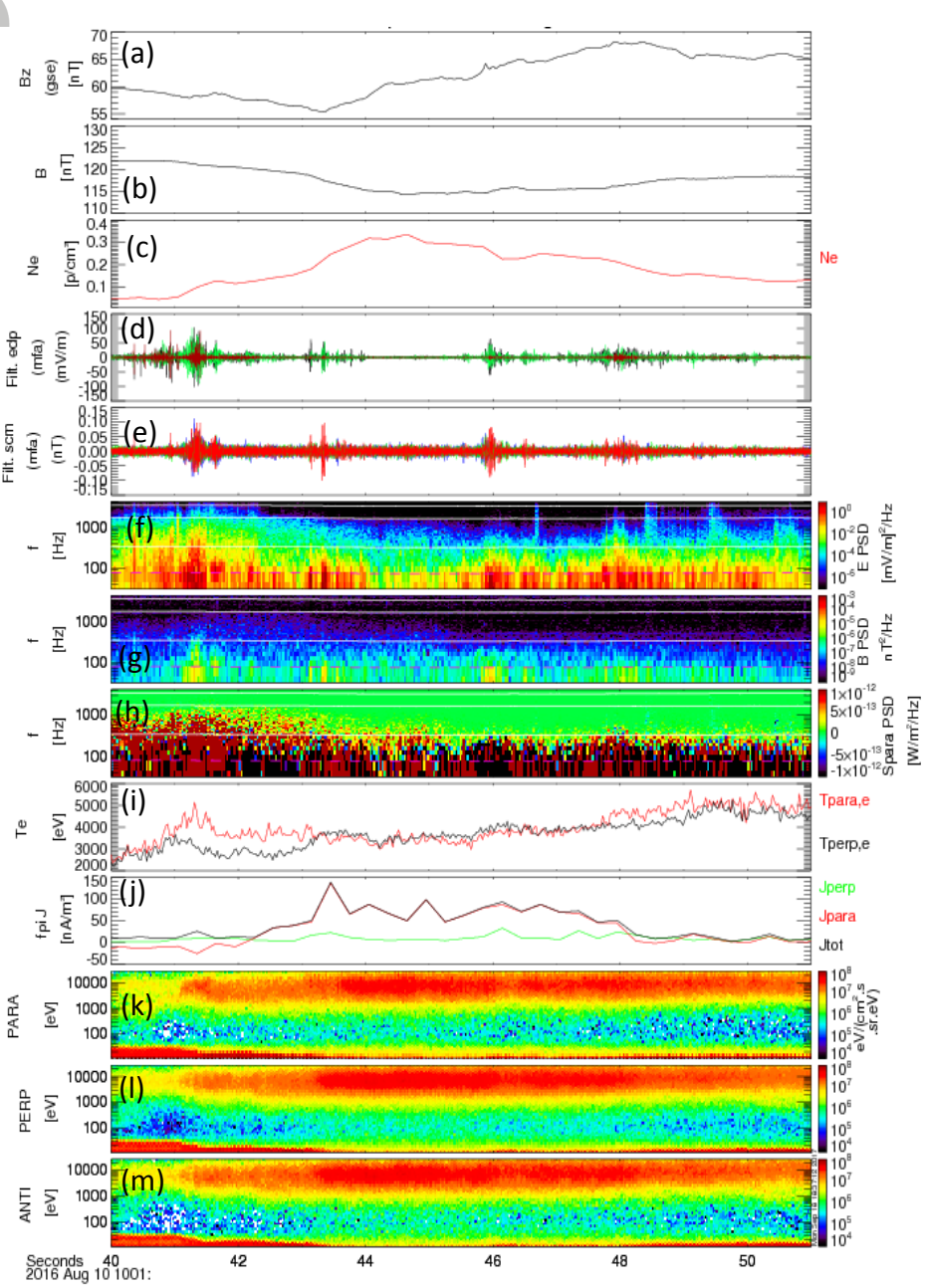

Figure 5. Second dipolarization front like signature detected by MMS3 between 1001:40.0 and 100151.0 UT. Same legend as Figure 4.

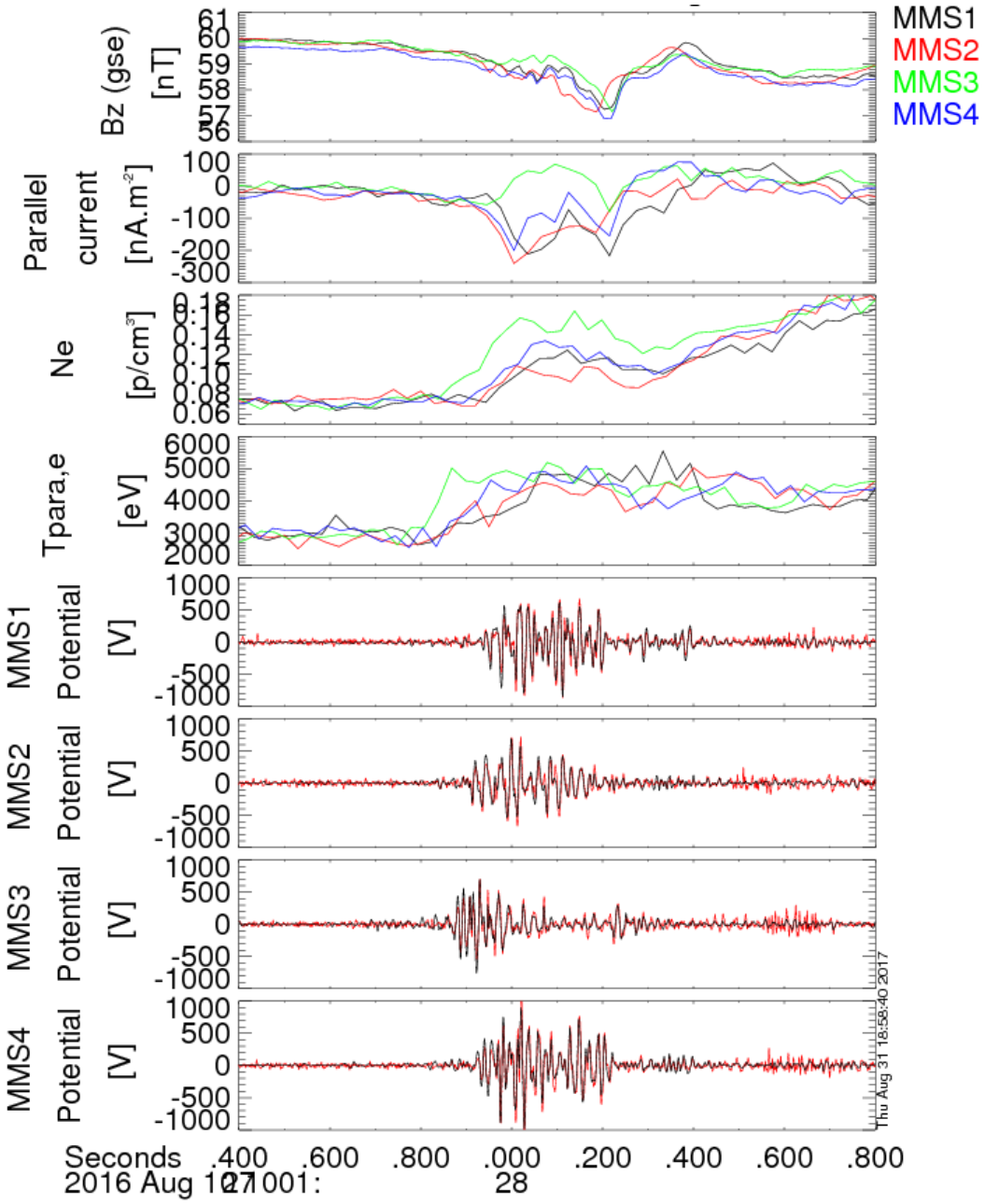

Figure 6. First dipolarization front like signature between 1001:27.400 and 100128.800 UT. From the four satellites: (a) B_z component in GSE, (b) parallel current, (c) electron density, electron parallel temperature, (e-h) electrostatic potential obtained from $\delta B_{\parallel}$ (red) and from $\delta E_{\perp}$ (black) for MMS1, MMS2, MMS3 and MMS4 respectively.

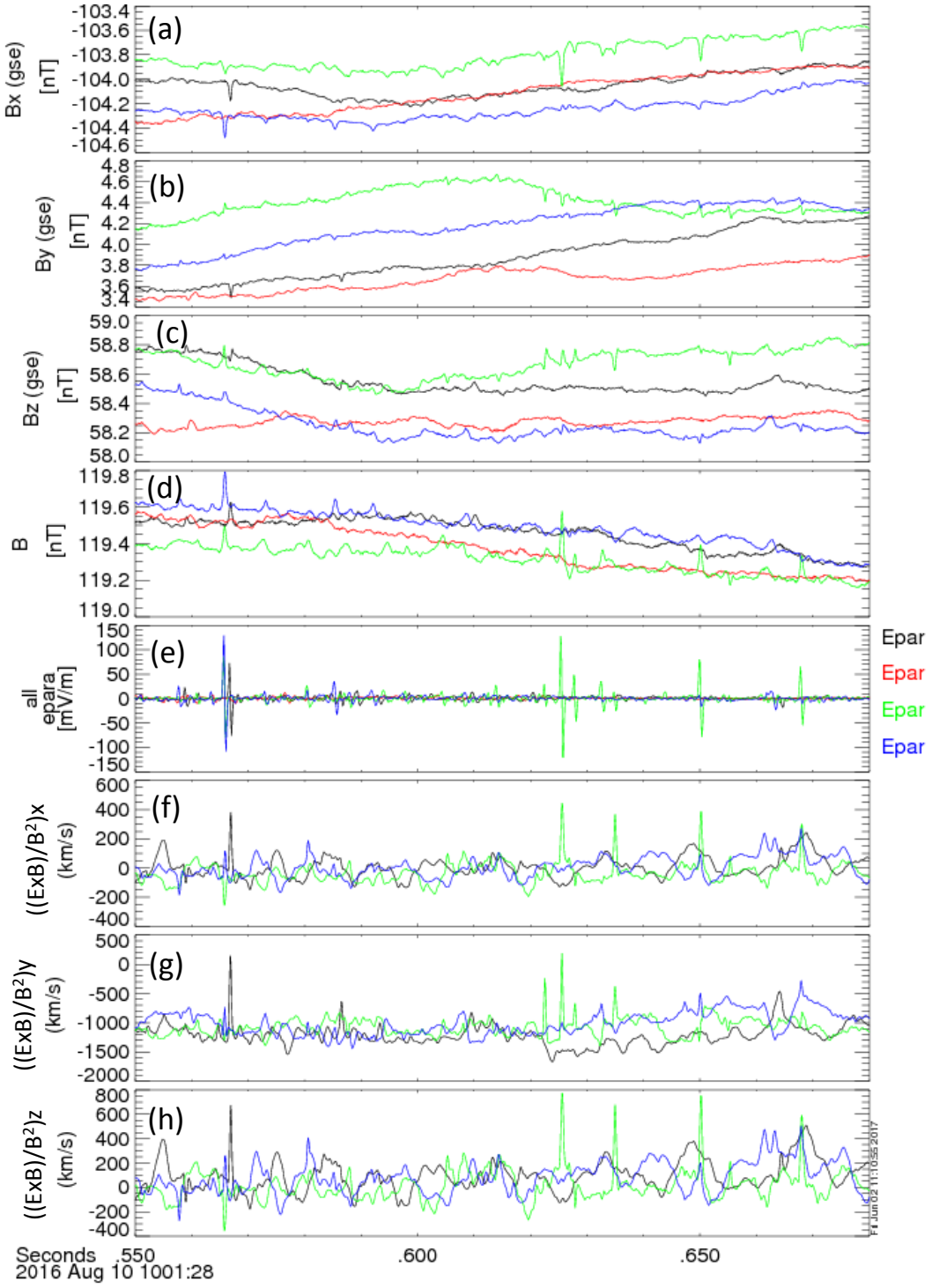

Figure 7. Electromagnetic phase-space holes associated with the first dipolarization front like signature between 1001:28.550 and 100128.680 UT. From the four satellites in GSE: (a-d) three components and magnitude of the magnetic field obtained from the merging of FGM and SCM data, (e) parallel electric field, (f-h) three components of the electric drift velocity $(\mathbf{E} \times \mathbf{B})/B^2$.

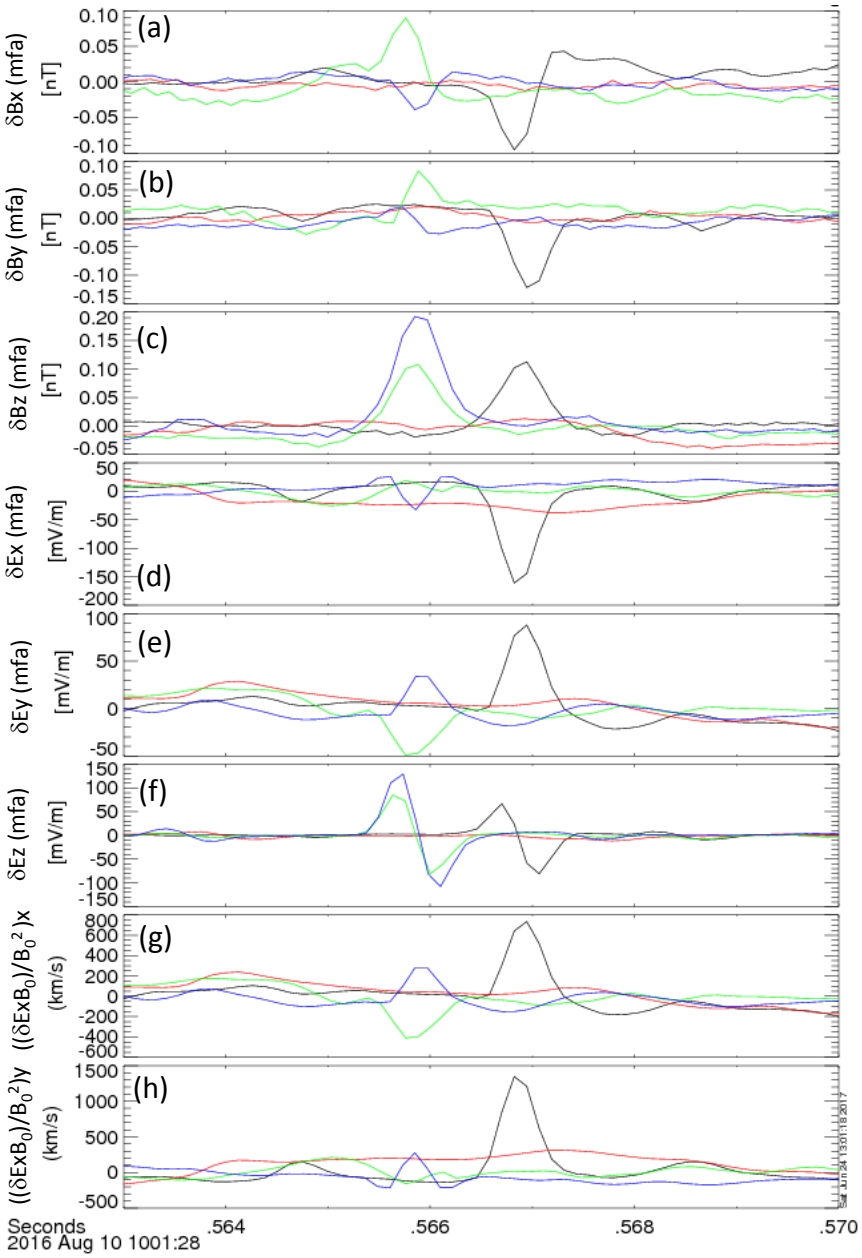

Figure 8. Single electromagnetic phase-space holes detected between 1001:28.563 and 1001:28.570 UT. From the four satellites in magnetic field-aligned coordinates and band-pass filtered between 32 Hz and 4 kHz: (a-c) three components of the magnetic field, (d-f) three components of the electric field, (g-i) two components of the electric drift velocity $(\delta\mathbf{E} \times \mathbf{B_0})/B_0^2$ in the two perpendicular directions of the MFA frame.

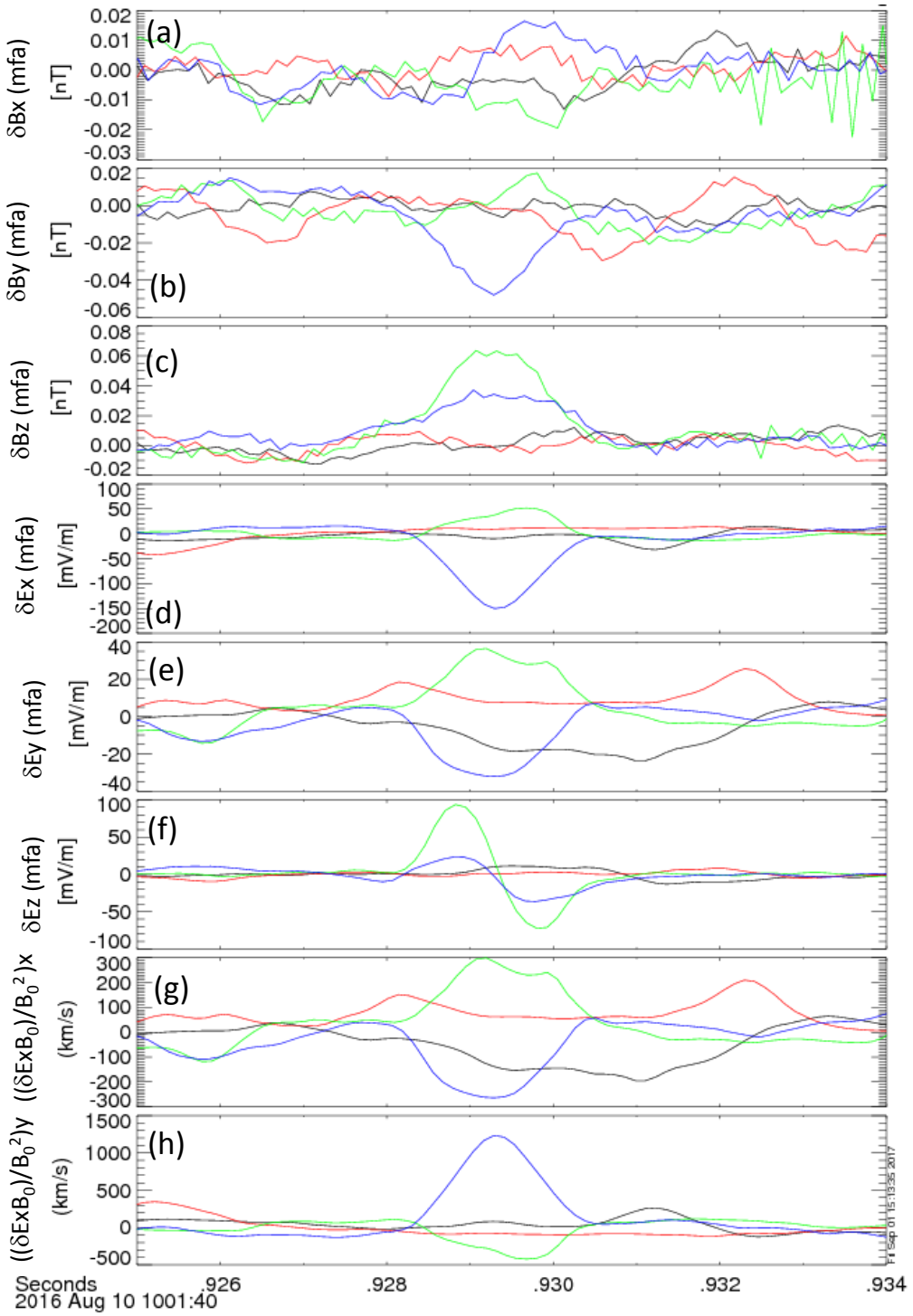

Figure 9. Single electromagnetic phase-space holes detected between 1001:40.925 and 100140.934 UT. Same legends as the Figure 9.

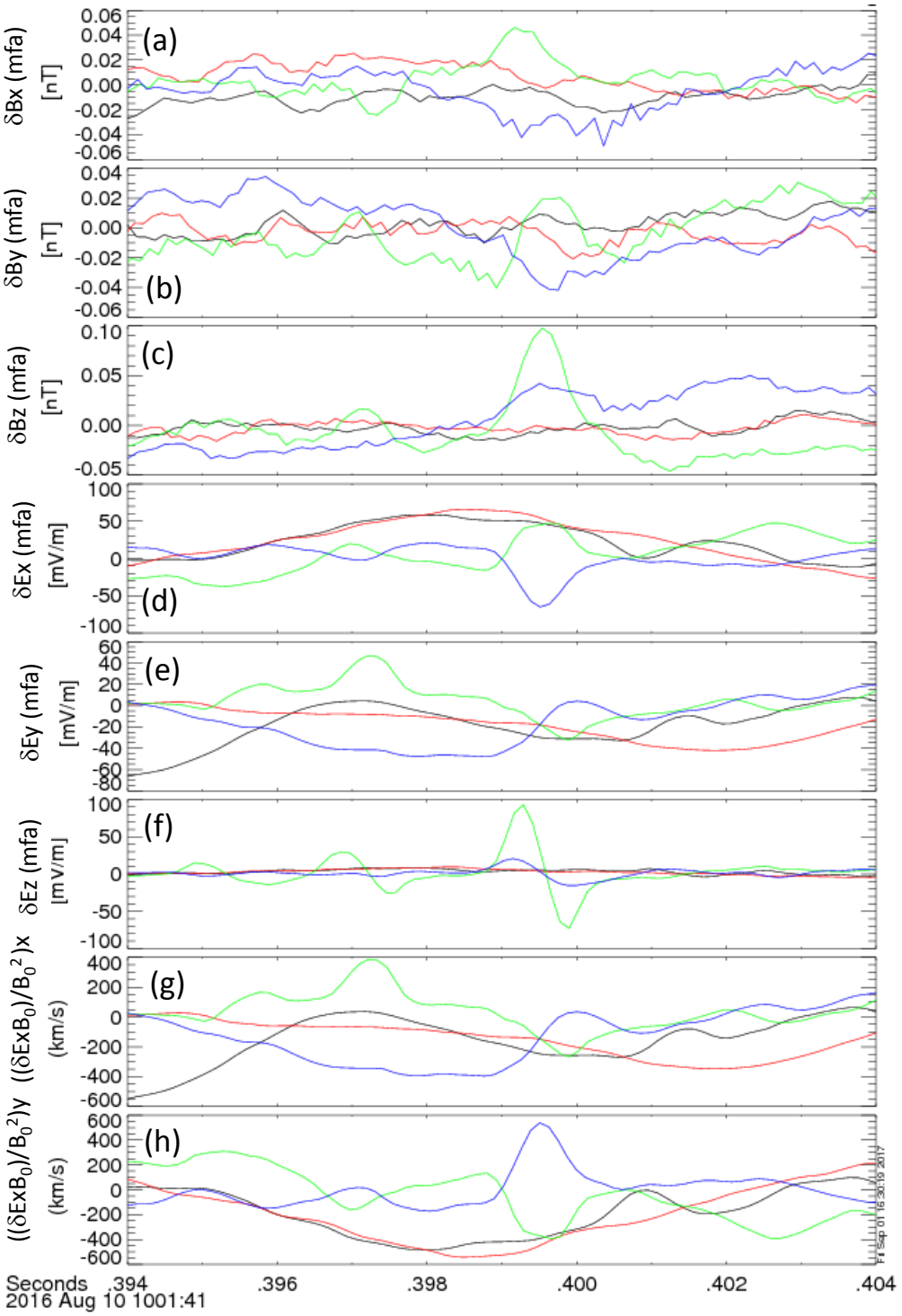

Figure 10. Single electromagnetic phase-space holes detected between 1001:41.394 and 1001:41.404 UT. Same legends as the Figure 10.

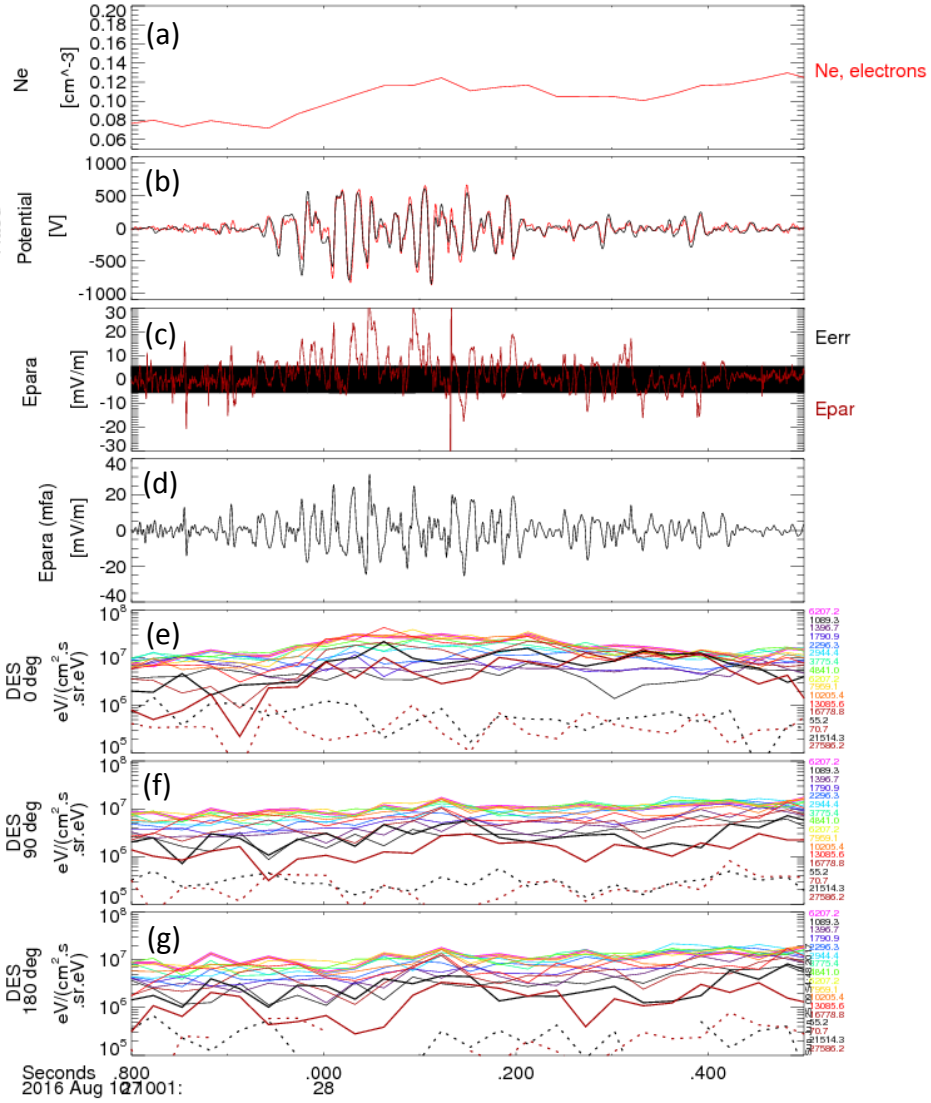

Figure 11. MMS1 measurements between 1001:27.800 and 1001:28.500 UT.Panel (a) electron density, (b) electrostatic potential obtained from $\delta B_{\parallel}$ (red) and from $\delta E_{\perp}$ (black), (c) parallel electric field calculated by using the DC-coupled EDP data and the survey magnetic field and its associated error bars, (d) band-pass filtered parallel electric in MFA frame, (e-g) FPI ion differential fluxes parallel, perpendicular and anti-parallel to **B** (see text for more details).